Robotics and Computer–Integrated Manufacturing 101 (2026) 103302

Contents lists available at ScienceDirect

Robotics and Computer-Integrated Manufacturing

journal homepage: www.elsevier.com/locate/rcim

Optimization of robotic machining through circular path error compensation

Kanglin Xing [a], J.R.R. Mayer [b], Yannick Cianyi [a], Ilian A. Bonev [c,*], Zhaoheng Liu [a], Henri Champliaud [a]

[a] Department of Mechanical Engineering, École de technologie supérieure, 1100 Notre-Dame St W, Montreal, Quebec, H3C 1K3, Canada
[b] Department of Mechanical Engineering, École Polytechnique (Montréal), P.O. Box 6079, H3C 3A7 Montréal, QC, Canada
[c] Department of Systems Engineering, École de technologie supérieure, 1100 Notre-Dame St W, Montreal, Quebec, H3C 1K3, Canada

ARTICLE INFO

Keywords:
Circular path error
Error compensation
Industrial robots
Ballbar
Laser tracker

ABSTRACT

Robotic machining offers flexibility and cost-efficiency, presenting a viable alternative to conventional machine tools. However, its inherently lower rigidity and repeatability often result in reduced machining accuracy. To improve machining quality, enhancements in robotic machining are typically achieved through parameter optimization, precision calibration, path error compensation, and process refinement. This study proposes an offline path error measurement and compensation strategy based on an out-of-plane ballbar method to address these challenges. An improved small-circle adaptor, combined with a Renishaw telescopic ballbar, was utilized to measure and compensate for circular path errors over a radius range of approximately 35 mm to 50 mm in both machining and non-machining conditions. For validation, a laser tracker was employed as a reference. Experimental results from robotic machining and ballbar measurement at the non-machining condition confirm the effectiveness of the proposed ballbar-based method in circular path error measurement and compensation. Specifically, for out-of-plane angle below 30° (corresponding to circular paths of radius between 43 mm and 50 mm), the new measurement method exhibited performance comparable to that of the laser tracker, as indicated by similar circular deviation ranges, consistent radial error patterns, surface roughness, circularity compensation rate exceeding 40% and a reduction in dimensional variation to less than 0.066 mm.

1. Introduction

Robotic machining offers enhanced flexibility and efficiency, enabling the processing of complex components with improved adaptability [1]. Accurate positioning is vital to the performance of industrial robots, especially in high-precision fields like manufacturing and aerospace. However, errors persist due to geometric issues such as inaccurate machining, assembly defects, and component wear. Non-geometric factors like elasticity, environmental fluctuations, limited control precision, and mechanical vibrations also contribute to these errors [2]. As a result, enhancing positioning accuracy remains a critical objective in the pursuit of improved robotic performance.

Positioning errors in industrial robots can cause deviations from the intended tool path, leading to imprecise machining and reduced product quality [3]. To improve robotic machining accuracy, various path error compensation strategies have been studied for industrial robots [3–5]. These methods are generally categorized into offline and online compensation approaches [6]. Offline error compensation primarily involves identifying the robots' kinematic parameters using tools such as laser trackers and coordinate measuring machines [7,8]. For example, a new systematic elastic model of the FANUC S420iF robot has been proposed, incorporating both geometric errors and elastic deformations [4]. This model optimizes the robot's trajectories in forming applications by compensating for tool center position (TCP) pose errors caused by structural flexibility. However, the effectiveness of offline path error compensation is limited by dynamic errors induced by thermal expansion, vibrations, and varying external loads [9]. In contrast, online error compensation strategies have been developed to account for these dynamic deviations in real time, thereby overcoming the inherent limitations of offline approaches. As a result, online compensation is typically integrated with offline calibration to enhance overall system accuracy. Depending on the measurement data sources and compensation mechanisms, online strategies can be classified into semi-closed-loop systems, which utilize joint position feedback, and fully closed-loop systems,

* Corresponding author.
E-mail address: ilian.bonev@etsmtl.ca (I.A. Bonev).

https://doi.org/10.1016/j.rcim.2026.103302
Received 2 July 2025; Received in revised form 9 February 2026; Accepted 13 March 2026
Available online 19 March 2026

which rely on end-effector or task-space feedback for enhanced accuracy. Commonly employed instruments for online closed-loop path error compensation include grating encoders [10], laser tracker [6,11] and dual-camera photogrammetry systems [12,13], all of which are utilized to detect pose-related deviations. Based on the acquired measurement data, a pose correction algorithm is implemented to precisely adjust the robot's trajectory toward the intended target position. Empirical evaluations of such compensation approaches on various robotic platforms have demonstrated high accuracy, with the Fanuc M20-iA achieving an absolute positioning deviation within ±0.05 mm [12], and the KUKA KR6 R700 exhibiting a mean single-point error of approximately 0.058 mm [6]. In addition, a novel real-time path correction approach based on joint position error (JPE) estimation and compensation with requiring only motor-side measurement and external wrenches was presented for ODG-JLRB20 industrial robot, a significant improvement (>80%) in the path accuracy was found [3].

Path error compensation techniques are generally applicable to a wide range of trajectory types, including linear segments, three-dimensional curves, and circular motions. Among these, circular trajectories are frequently utilized in robotic machining processes involving boss-like and concave geometries. To ensure high-quality machining of such components, accurate detection of path deviations is essential. The measurement of circular path errors can be conducted using various instruments, such as laser trackers, photogrammetry systems, or ballbar devices, each offering reliable pose evaluation for error compensation purposes [14]. The accuracy of laser trackers and photogrammetry is influenced by their operating range, with typical resolutions around 8.8 μm for the FARO laser tracker and volumetric accuracies near 65 μm for the C-Track 780. In contrast, the ballbar demonstrates a distinct advantage in terms of sensor resolution—such as ±0.01 μm in the case of the Renishaw system—as well as in operational simplicity and cost efficiency. Nonetheless, the ballbar is constrained to a limited set of circular path diameters, including 50 mm, 100 mm, 150 mm, and 300 mm. The effectiveness of circular path error compensation is influenced by multiple parameters, including the choice of measurement instrument, the compensation technique implemented, and the sampling frequency of the data acquisition system. Differences in resolution and functionality among available tools highlight the importance of selecting appropriate equipment for use in practical, shop-floor environments. Despite ongoing advancements, a unified strategy for circular path error compensation that systematically considers these interrelated factors is still lacking. In addition, formalized procedures for deploying ballbar devices for general circular path error assessment and correction have yet to be established.

Although optical metrology systems are capable of providing full 3D task space coordinates, they pose practical limitations for routine deployment in robotic machining cells. The achievable accuracy of a laser tracker depends strongly on the measurement volume and setup and is sensitive to line-of-sight interruptions, reflector mounting stiffness, and environmental effects such as thermal drift. In addition, laser tracker-based compensation typically requires dedicated installation space, careful frame registration, and high equipment and operation costs. Vision based photogrammetry systems are often easier to deploy, but their accuracy and robustness can be affected by camera calibration quality, illumination changes, occlusions, and marker detection, and their volumetric accuracy is commonly in the range of several tens of micrometers in typical shop-floor volumes. These constraints motivate a complementary, low-cost, and rapidly deployable measurement approach for circular path verification and compensation. In particular, for circular trajectories with radii that do not match the discrete nominal diameters of conventional ballbar systems, a practical and systematic approach is needed to extend ballbar based assessment to continuously variable circular paths under shop-floor constraints, as summarized in Appendix F.

In light of the above considerations, an offline circular path error compensation strategy for robotic machining using a ballbar angular setup method is proposed in this paper. A ballbar configured with an out-of-plane angle is proposed for the measurement of path errors across a range of radii, instead of being restricted to standard radii. Both theoretical analysis and experimental evaluation were conducted to investigate the accuracy of circular path error measurement with the proposed out-of-plane ballbar method (Fig. 2) angles. The effectiveness of the proposed method was validated through robotic machining trials on a cylindrical aluminum workpiece. The findings provide a foundational basis for the development of future online circular path error compensation strategies using both ballbar and laser tracker systems within a hexapod-based machining platform. Although the validation in this study is primarily conducted on a hexapod platform, the proposed out-of-plane ballbar method is conceptually applicable to other robotic architectures such as serial manipulators and SCARA robots, provided that the out-of-plane angle is controlled within the recommended range (≤30°). The remainder of this paper is organized as follows: the subsequent section introduces the methodologies for circular path error measurement and compensation using out-of-plane ballbar measurement method; Section 3 introduces the path error compensation strategies for ballbar and laser tracker; Section 4 describes the experimental configuration; Sections 5 presents the experimental results and their analysis; Section 6 discusses the results and Section 7 concludes with a summary and potential directions for further research.

2. Out-of-plane ballbar method for circular path error measurement

The ballbar is a precision measurement device used for the rapid performance testing and verification of machine tools or industrial robots (Fig. 1(a)). It comprises a precision linear sensor and two precision balls positioned at its ends. Variations measured along a predefined circular path in a 2D plane, under specified feed speeds and testing radius at the clockwise (CW) and counter-clockwise (CCW) directions (Fig. 1(b)), are analyzed to calculate machine tool errors. Common testing radius for ballbar measurements include 50 mm, 100 mm, 150 mm, and 300 mm. The raw path error (PE_r) is defined as the difference between the actual circular path and the nominal circular path (Eq. 1). This error, measured by the ballbar, is processed using a least-squares fitting method to determine the precise rotation center. Subsequently, the true radial error is analyzed using specific models to calculate multiple machine error parameters and circular deviation. The current ballbar system is primarily designed for precision measurement of machine tools. However, the processed data from ballbar software cannot be directly applied to circular path error measurements due to its insufficient and inconsistent sampling rate. For instance, the Renishaw ballbar system, while offering a maximum sampling rate of 1000 Hz, experiences variations in actual sampling rate depending on the feed speed. Nevertheless, the Renishaw-provided Automatic Programming Toolkit (APT) allows the ballbar to capture circular path errors accurately at a constant sampling rate of 1000 Hz [15]. This setup ensures a sufficient quantity of circular path error data, enabling effective path error compensation.

2.1. Out-of-plane ballbar principle and configuration

The commercial ballbar system, being limited to a few fixed lengths (e.g., 50 mm, 100 mm, 150 mm, and 300 mm), is of limited use for in-plane circular path error measurement and compensation, where the ballbar axis remains within the same plane. However, actual machining processes involve cylinders and holes of varying dimensions, requiring a more versatile path error measurement and compensation capability. To address this need, an out-of-plane measurement and data processing approach is proposed and validated in this study (Figs. 1 and 2). By following a circular path with a radius smaller than the ballbar length, thereby moving the ballbar along a conical surface rather than confining it to a single plane, a method for measuring path errors along various

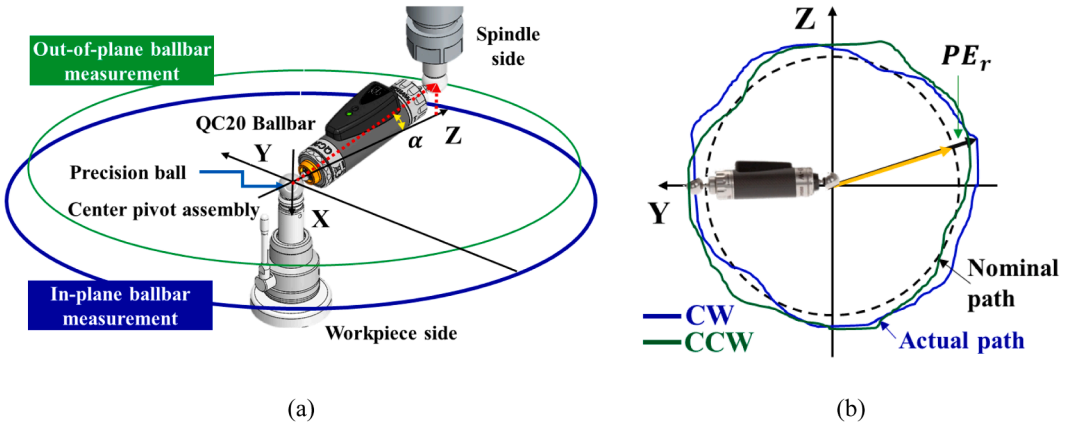

Fig. 1. Ballbar measurement system: (a) Setup for circular path error measurement using in-plane and out-of-plane ballbar measurement method; (b) Path error measured by ballbar on the CW and CCW directions. It is worth noting that the coordinate system shown here is aligned with the experimental platform to ensure consistency throughout the description.

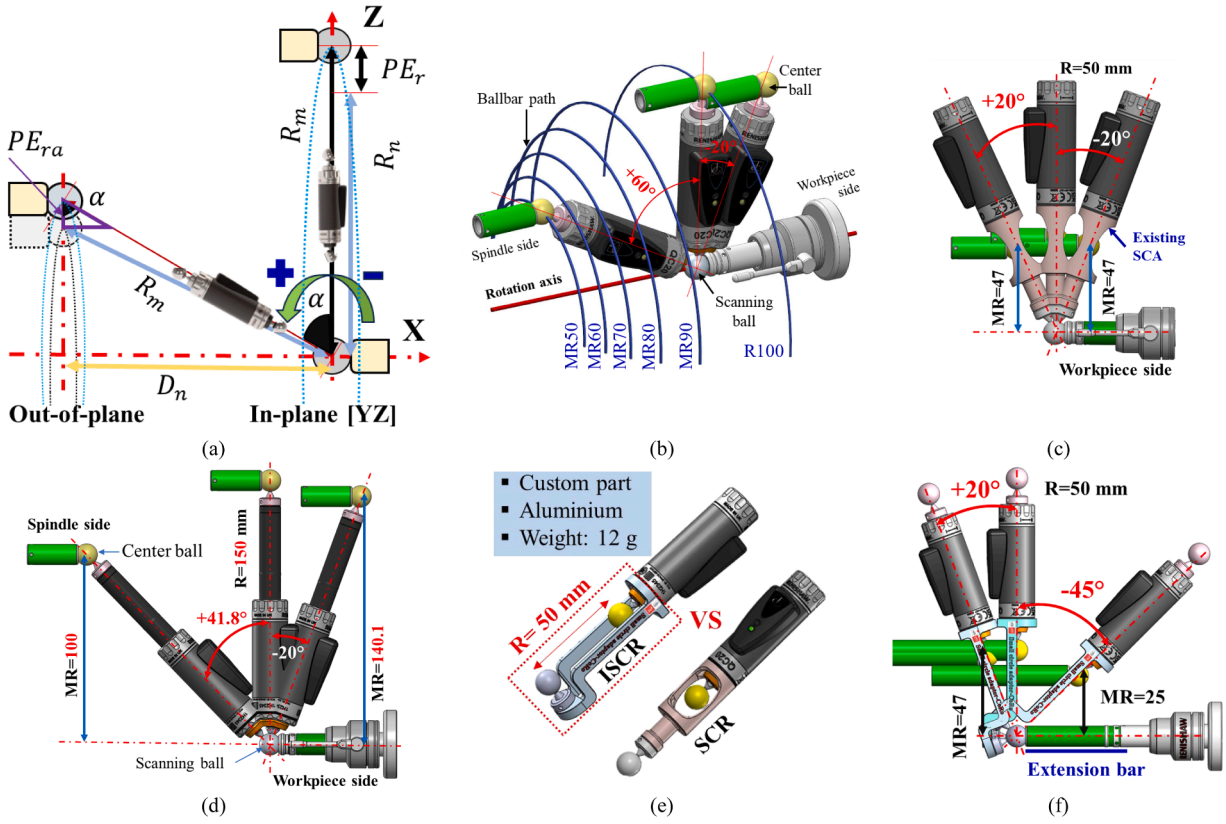

Fig. 2. A novel ballbar measurement setup and comparison of in-plane and out-of-plane configurations: (a) Theoretical path error measured using out-of-plane and in-plane ballbar methods, where red dashed line with the red dot indicates the reference axis of the nominal circular trajectory, used to distinguish between in-plane and out-of-plane configurations. The out-of-plane configuration forms an angle α with this axis; (b) Out-of-plane measurement range for the 100-mm ballbar, with MR representing the measured radius under the out-of-plane configuration; corresponding to the sub-figures below; (c) Out-of-plane measurement range for a 50-mm ballbar with the existing small-circle adaptor (SCA); (d) Out-of-plane measurement range of a 150-mm ballbar; (e) The proposed improved small-circle adaptor (ISCA) and the existing SCA; (f) installation and out-of-plane measurement range using the new 50-mm ISCA.

circular paths is introduced (Fig. 2(a and b)). This method will be referred in the rest of the paper as out-of-plane ballbar measurements.

The out-of-plane measurement can be performed with either the positive or negative out-of-plane angle (Fig. 2(b)). The choice of out-of-plane direction accounts for potential interferences between the ballbar and the so-called center pivot assembly, as well as the relative position of the cutter to the workpiece for machining purpose. Typically, a positive direction helps minimize interferences between the ballbar and the pivot assembly; however, it may result in the cutter being positioned at a relatively greater distance from the workpiece, particularly when using a ballbar with a large length. Conversely, a negative direction allows the cutter to be closer to the workpiece but may introduce interference, especially when employing a ballbar with a length of 50 mm (Fig. 2(d)). Following this principle, the ballbar out-of-plane direction can be selected with the balance of the potential interference and machining need.

For the existing ballbar with a specific length, the selection of out-of-plane angles (α) and the measurable radius are outlined as follows:

1) Ballbars with nominal length of 100 mm and 150 mm can be consolidated into a single type, as minimal interference is observed between the ballbar and the pivot assembly, or the connection bar installed on the spindle. A ballbar with a nominal length of 100 mm is capable of measuring radius ranging from 50 mm to 100 mm at out-of-plane angles of +60° and -20° (Fig. 2a). Similarly, a ballbar with a nominal radius of 150 mm can measure radius ranging from 100 mm to 150 mm, with out-of-plane angles between +41.8° and -20° (Fig. 2(c)). Although the maximum angle in the positive direction can theoretically reach 90°, installation errors can significantly influence the final compensation results, as demonstrated in the next section. Consequently, the effective range of ballbar out-of-plane angles is presented within this constraint in mind.
2) The existing small-circle adaptor (SCA), designed for in-plane circular paths of 50 mm in radius, has a limited out-of-plane angular range (approximately ±20°) due to its mechanical structure, thereby restricting out-of-plane measurements to radii no smaller than 47 mm.
3) For the ballbar with length of 300 mm, its the range of measurement range radii could be extended from 150 mm to 300 mm with out-of-plane the installation angles of between +45° and −20°.

Given the typical dimensions of holes on workpieces, the 50 mm length ballbar is most commonly required. To address the measurement limitations associated with the existing SCA, an improved small circle adaptor (ISCA) was developed (Fig. 2(e and f)). Detailed structural drawings, dimensions, tolerances, and material specifications of the ISCA are provided in Appendix A. The adaptor extends the measurement range of the existing ballbar from a fixed value of 50 mm to an adjustable range of 35–50 mm, thereby permitting out-of-plane measurements at angular deviations between +45° and −20°. For its installation, one end of the adaptor connects to the center ball, while the other end attaches the ballbar body to the center ball via threaded connections. Subsequently, the distance between the scanning ball and the center ball can be fixed at 50 mm. In addition, the standard QC-20W ballbar used in this study has a core length of 100 mm. Renishaw also provides extension bars of 50 mm, 150 mm, and 300 mm, which can be combined with the ballbar or the SCA to enable testing at radii of 50, 100, 150, 250, 300, 400, 450, 550, and 600 mm. Calibration can be verified using Renishaw-provided calibration plates for the 50, 150, and 300 mm configurations.

For the general ballbar length, the measured path error PE_r can be easily processed for path error compensation PE_c (Eqs. 1 and 2, where R_m and R_n stands for the measured radius and the nominal radius, respectively). As for the ballbar-angle setup, out-of-plane angle α is included for the calculation of path error (PE_{ra}) under this setup (Eqs. 3, 4 and 5, where D_n stands for the normal distance under angular setup). When α=0°, the ballbar operates as it does in standard measurements, with $PE_{ra} = PE_r$.

$$PE_r = R_m - R_n \tag{1}$$

$$PE_c = -PE_r \tag{2}$$

$$D_n = sin(\alpha)\cdot R_n \tag{3}$$

$$PE_{ra} = \sqrt{R_m{}^2 - D_n{}^2} - cos\ (\alpha)\cdot R_n \tag{4}$$

$$PE_c = -PE_{ra} \tag{5}$$

2.2. Visibility and blind direction analysis for out-of-plane ballbar measurements

To evaluate the observability of radial deviation in out-of-plane ballbar measurements, this section establishes a generalized model that characterizes how the measurable component varies throughout the entire circular trajectory. The method is based on a directional analysis of the ballbar's real-time orientation, and utilizes Gram–Schmidt orthogonalization [16] to decompose the radial deviation vector into two orthogonal components: one aligned with the ballbar direction (measurable) and the other lying in the same plane as the radial deviation and orthogonal to the ballbar. While an infinite number of directions are mathematically orthogonal to the ballbar, this particular blind direction is chosen for its physical relevance, as it directly captures the unobservable component of the radial deviation in the plane of motion. This framework enables a quantitative description of visibility loss introduced by different out-of-plane configurations. In this model, $\widehat{b}(\theta)$ represents the unit direction vector of the ballbar at angular position θ, corresponding to its real-time spatial orientation as the circular path is executedIn this model, the angular parameter θ is defined as increasing clockwise from the positive Z-axis. The ballbar is tilted at a fixed angle α toward the negative X-axis, forming a conical surface in three-dimensional space. The instantaneous direction of the ballbar at angular position θ (Fig. 3 (a)), when tilted by an angle α from the nominal Z-axis, is given by the following unit vector:

$$\widehat{b}(\theta) = \begin{bmatrix} -sin(\alpha) \\ cos(\alpha)\cdot sin(\theta) \\ cos(\alpha)\cdot cos(\theta) \end{bmatrix} \tag{6}$$

This vector represents the real-time direction along which the ballbar length is measured. As θ progresses from 0° to 360°, the ballbar direction rotates accordingly in 3D space, while remaining confined to a conical surface defined by the tilt angle α. To simulate circular path errors, the instantaneous deviation is assumed to occur purely along the radial direction of the circular path. $\widehat{V_r}(\theta)$ denotes the unit vector pointing along the instantaneous radial deviation direction within the YZ plane and it is written as:

$$\widehat{V_r}(\theta) = \begin{bmatrix} 0 \\ sin(\theta) \\ cos(\theta) \end{bmatrix} \tag{7}$$

This deviation vector always lies within the YZ plane and varies with θ, reflecting the nature of rotary path deviation from the ideal circle center. To determine the component of the radial deviation that is undetectable by the ballbar, we construct a direction vector strictly orthogonal to $\widehat{b}(\theta)$. This is accomplished through the Gram-Schmidt orthogonalization process:

$$\widehat{b}_{\perp}(\theta) = \frac{\widehat{V_r}(\theta) - (\widehat{V_r}(\theta)\cdot\widehat{b}(\theta))\cdot\widehat{b}(\theta)}{\| \widehat{V_r}(\theta) - (\widehat{V_r}(\theta)\cdot\widehat{b}(\theta))\cdot\widehat{b}(\theta)\|} \tag{8}$$

This ensures that $\widehat{b}_{\perp}(\theta)$ is completely perpendicular to $\widehat{b}(\theta)$ and lies in the same plane spanned by $\widehat{b}(\theta)$ and $\widehat{V_r}(\theta)$. Geometrically, it corresponds to the direction along which the ballbar is entirely insensitive. The measurable component of the radial deviation is the projection of $\widehat{V_r}(\theta)$ onto the ballbar direction:

$$MC(\theta) = \widehat{V_r}(\theta)\cdot\widehat{b}(\theta) \tag{9}$$

This scalar represents the magnitude of the deviation that can be detected and quantified by the ballbar system. The blind component is the projection of $\widehat{V_r}(\theta)$ onto the orthogonal direction $\widehat{b}_{\perp}(\theta)$, which cannot be captured by ballbar measurement:

$$BC(\theta) = \widehat{V_r}(\theta)\cdot\widehat{b}_{\perp}(\theta) \tag{10}$$

To visualize the angular dependence of the measurable and blind components introduced in Eqs. 9 and 10, numerical simulations were carried out for multiple out-of-plane angle α, with results presented in Fig. 3 (b) through (d). Fig. 3 (b) illustrates the projection of the radial

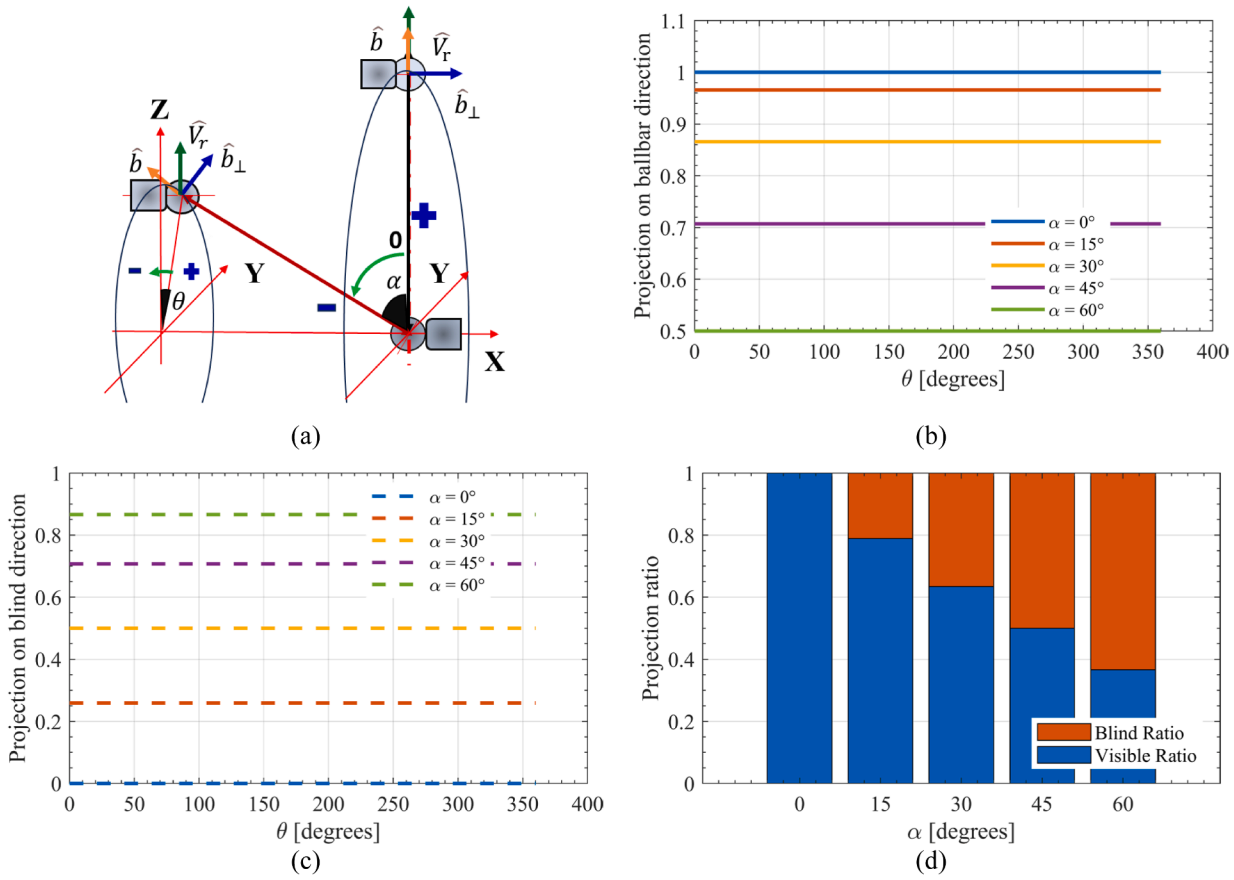

Fig. 3. (a) Error projected on the ballbar measurement direction and the blind direction; (b) Projection of the radial deviation vector $\widehat{V_r}(\theta)$ onto the ballbar direction $\widehat{b}(\theta)$ as a function of angular position θ (Eq. 9). Solid curves indicate different out-of-plane angles α= 0°, 15°, 30°, 45°, and 60°; (c) Projection of the radial deviation vector $\widehat{V_r}(\theta)$ onto the blind direction $\widehat{b}_{\perp}(\theta)$obtained via Gram-Schmidt orthogonalization (Eq. 10); (d) Cumulative visibility and blindness ratio of radial deviations across a full circular path (θ=0°-360°) for various tilt angles. The visible area is calculated as the integral of Eq. 11, while the blind area corresponds to Eq. 12.

deviation vector $\widehat{V_r}(\theta)$ onto the real-time ballbar direction $\widehat{b}(\theta)$. This projection quantifies the instantaneous measurable component. When α=0°, the deviation vector aligns fully with the ballbar direction across the entire circular path, leading to perfect sensitivity. As α increases, this alignment degrades, and the projection amplitude decreases. The curves flatten and fall as α increases, confirming a monotonic reduction in instantaneous measurement sensitivity. Fig. 3 (c) presents the projection of $\widehat{V_r}(\theta)$ onto the blind direction $\widehat{b}_{\perp}(\theta)$, which is computed using Gram-Schmidt orthogonalization to ensure strict orthogonality with $\widehat{b}(\theta)$. Since this direction is strictly orthogonal to the ballbar orientation, the projection captures the portion of the radial deviation that remains unmeasurable. As α increases, the blind projection grows steadily, reflecting the trade-off introduced by out-of-plane angle α: while enabling spatial flexibility, it simultaneously increases the fraction of information lost to the ballbar system.

To evaluate the overall sensitivity loss, the projection area ratio (visible ratio-blind ratio) is introduced. This metric aggregates the projection amplitudes over the entire circular path, offering a normalized visibility metric:

$$\text{Visible\_ratio} = \frac{\int_0^{2\pi} |\widehat{V_r}(\theta)\cdot\widehat{b}(\theta)|\mathrm{d}\theta}{\int_0^{2\pi} (|\widehat{V_r}(\theta)\cdot\widehat{b}(\theta)| + |\widehat{V_r}(\theta)\cdot\widehat{b}_{\perp}(\theta)|)\mathrm{d}\theta} \tag{11}$$

$$\text{Blind\_ratio} = \frac{\int_0^{2\pi} |\widehat{V_r}(\theta)\cdot\widehat{b}_{\perp}(\theta)|\mathrm{d}\theta}{\int_0^{2\pi} (|\widehat{V_r}(\theta)\cdot\widehat{b}(\theta)| + |\widehat{V_r}(\theta)\cdot\widehat{b}_{\perp}(\theta)|)\mathrm{d}\theta} \tag{12}$$

Fig. 3 (d) summarizes these ratios for a range of out-of-plane angles. As α increases from 0° to 60°, the visible area ratio decreases monotonically, while the blind area grows. Notably, at α=30°, approximately 63.4% of the radial deviation remains measurable, while the remaining 36.6% becomes invisible to the system. This represents a meaningful inflection point: beyond 30°, the degradation in measurement performance accelerates significantly. Thus, from both theoretical analysis and practical considerations, limiting the out-of-plane angle to 30° or less is recommended as a balanced compromise. It maintains acceptable observability while still enabling flexible spatial configurations in robotic calibration or small-radius testing setups. This visibility modeling, based on Gram–Schmidt orthogonalization, represents a new theoretical framework for quantifying the observability limits of out-of-plane ballbar measurements, which has not been explicitly addressed in prior optical or laser-based systems.

2.3. *Theoretical modeling of out-of-plane angle and assembly error*

The out-of-plane measurement approach extends the effective application range of the ballbar system, reducing the minimum testable radius from 50 mm to 35 mm. However, the theoretical error associated with the ballbar and the assembly error of the improved small-circle adaptor may introduce additional inaccuracies in the ballbar path error measurement (Fig. 4). The theoretical error arises due to the installation method, as the measurement is transformed from a two-dimensional (2D) configuration into a three-dimensional (3D) configuration. For a given out-of-plane angle, the ballbar readings can be influenced by changes occurring at several positions. Ideally, it is assumed that variations in the ballbar readings can be attributed to a

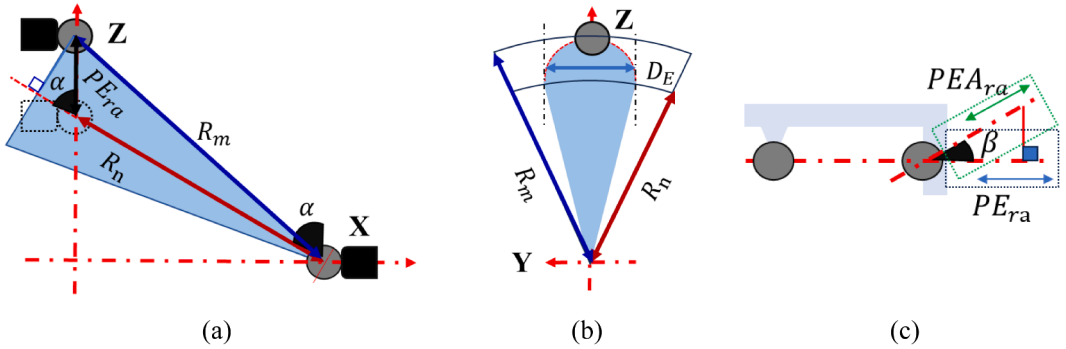

Fig. 4. Theoretical error originated from out-of-plane ballbar method: (a) Error modeling of ballbar under out-of-plane ballbar setup (Front View); (b) Error modeling of the ballbar under out-of-plane ballbar setup (Right View), the three-dimensional visualization of the uncertainty envelope D_E across varying tilt angles α; (c) Error modeling of the ballbar with the improved small circle adaptor under assembly reflecting the geometric interpretation of radial deviation projection in an out-of-plane ballbar configuration.

single specific theoretical position in the ballbar data processing since the measurement is conducted on one 2D plane. In practice, however, this assumption is not always valid. For the measured ballbar radius (R_m), the assumed radial error (PE_{ra}) under angular setup is changed along the Z-axis (Fig. 4 (a)). While in the 3D space, the true radial can be generated by multiple positions, these positions can be distributed into a circle and forms a 3D cone (Fig. 4 (b)). This 3D cone is generated by rotating the instantaneous radial deviation around the nominal circular path, and represents the spatial uncertainty envelope due to out-of-plane angle. The vertical spread of each surface is governed by the magnitude of the true radial deviation, while the horizontal spread (cone radius) depends on both α and the nominal ballbar radius. As α increases, the projection of the deviation vector onto the ballbar direction becomes less sensitive, and the spatial region that could generate an identical reading grows accordingly. In the side view of Fig. 4 (a), the projected distribution of radial error positions forms a bounded area, denoted D_E (uncertainty range). This region reflects the angularly-induced uncertainty cone shown in Fig. 4 (b), and its extent depends on the out-of-plane angle (α), the nominal radius L, and the radial deviation amplitude (PE_{ra}) under the configured setup. It can be modeled as Eq. 13.

$$D_E = 2{\cdot}cos\ (\alpha){\cdot}PE_{ra} = 2{\cdot}cos\ (\alpha){\cdot}\left(\sqrt{{R_m}^2 - {D_n}^2} - sin\ (\alpha){\cdot}PE_n\right) \tag{13}$$

Using ballbar with the length of 50 mm, 100 mm, and 150 mm as examples, when the radial error PE_{ra} is set to 0.1 mm, the variation in ballbar measurements under different out-of-plane angles and their ratios relative to the total perimeter of the ballbar circle are shown in Fig. 5. The maximum measurement uncertainty occurs at the maximum out-of-plane angle of 60°. Minimal differences are observed across the various ballbar lengths. Consequently, a small installation angle for the ballbar is recommended.

Regarding the installation error of the improved small circle adaptor, discrepancies in machining or assembly precision may result in misalignment between the axis of the ballbar measurement direction and the axis of the adaptor, forming an angle (β) (Fig. 4 (c)). Consequently, the measured result will exceed the actual error value. When β is known, the actual measured radial error can be calculated as

$$PEA_{ra} = Cos\ \beta{\cdot}PE_{ra} \tag{14}$$

Where PE_{ra} denotes the true radial deviation magnitude, while PEA_{ra} represents the measurable projection along the ballbar axis.

In practice, the determination of β can be conducted experimentally through the following procedure. First, calibrate the ballbar using both the improved and Renishaw-provided small circle adaptors with the Renishaw-supplied calibration pad. Next, set up two balls (scanning and center balls) at several fixed distances. Measure the distance between the two balls using the ballbar equipped with the improved small circle adaptor and, separately, with the Renishaw-provided small circle adaptor. Finally, calculate the angle β using the measurement results from the two adaptors and Eq. 14. The paired calibration procedure, regression model, and statistical confidence bounds of β are reported in Appendix B.

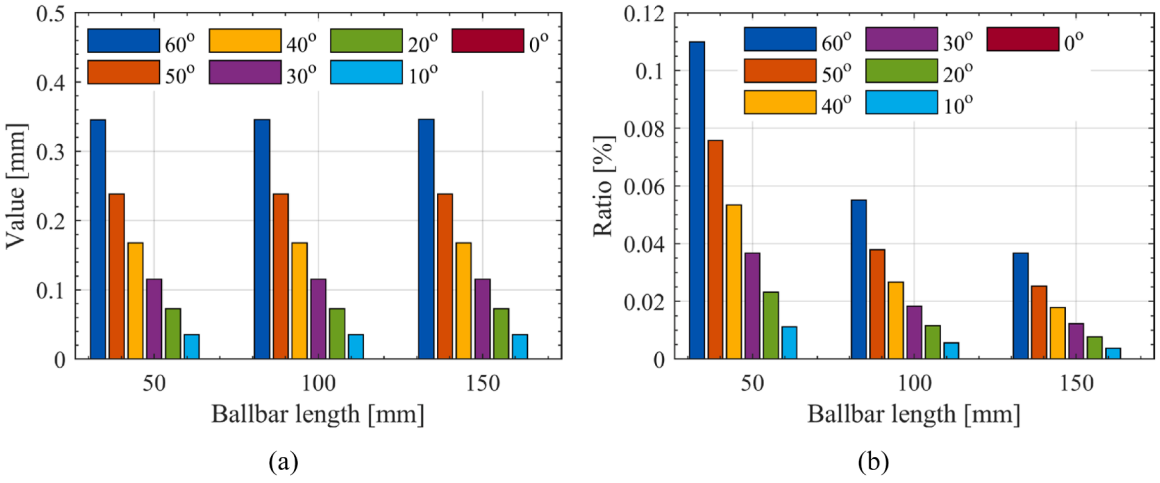

Fig. 5. Uncertainty of the out-of-plane ballbar method: (a)The uncertainty of ballbar installed under angular setup; (b) Ratio of the unexpected change related to the perimeter of ballbar.

3. Path error compensation strategy

3.1. Offline path error compensation using ballbar

Online and offline error compensation methods are commonly employed for circular path error correction. The choice of method depends on factors such as the circular motion generation technique and the ballbar sampling rate. In robotic circular motion planning, two primary approaches are typically used: point-to-point (Fig. 6 (a), green points) and continuous-path methods [17]. The point-to-point method is the simplest approach, generating a circular trajectory by connecting numerous small linear segments. However, this method introduces feedrate fluctuations at junction points, resulting in sharp trajectories and unwanted vibrations [18]. In practice, several solutions could be used against these limitations. These include trapezoidal or bell-shaped velocity profiles (utilizing cubic, quartic, or quintic polynomials) [19] and advanced control strategies that account for joint variables and velocity vectors [17]. In contrast, continuous-path methods, such as circular arc motion and circular motion commands for FANUC robots (Fig. 6), are more widely used. These commands utilize arc segments as the fundamental elements for generating a complete circle. The circular arc motion method offers enhanced control for applications requiring precise customization of arcs (Fig. 6 (a), orange colour), while circular motion commands provide a simpler approach for defining circular trajectories using a minimum of five geometric points (Fig. 6 (b)). Finally, the selection of the appropriate circular path generation method should consider criteria such as runtime, energy consumption, and the smoothness of the motion path [20,21].

Different path error compensation strategies can be applied based on the characteristics of circular path generation methods. The point-to-point method and circular arc motion method are well-suited for offline path error compensation, as they allow a large number of path errors associated with each control point to be generated and subsequently applied to the respective control points. For the circular motion method, a minimum of five control points is required. However, this limited number of control points makes it challenging to accommodate the large number of measured path errors. As a result, this method is better suited for online path error compensation. In this study, the circular arc motion method was employed for circular path error measurement using a ballbar. Consequently, the offline circular path error compensation method was implemented. Future work will propose an online path error compensation method that integrates the dynamic path modification (DPM) function of the FANUC robot for the application of the proposed technique. Once the path error compensation method is selected, the subsequent data processing will be performed.

For the calculated compensation error $Compe_i$ with a dimension of N (i=1,2,…,N), when the offline path error generation method employs N1 control points for circular path generation at the YZ plane, the compensation value for each control point along Y and Z axis and the new coordinates of the control positions are calculated as the following equations 15 to19. Given that the sampling rate for the ballbar is 1000 Hz, the calculated compensation errors will far exceed the number of control points (N1) used to define the circular path. To address this, the calculated compensation errors are evenly divided into segments, and the mean value of each segment is computed (Eq. 17). Finally, the compensated control-point coordinates computed from Eqs. (18)–(19) are used to update the FANUC circular program by replacing the nominal point list for offline path error compensation.

$$A = \mathrm{round}(N / N1) \tag{15}$$

$$\alpha = 360^{\circ}/N1 \tag{16}$$

$$PEc_j = \mathrm{mean}\left(PEc_{1+A*(j-1)} : PEc_{A+A*(j-1)}\right)\ j\ \epsilon\ [1,\ N1] \tag{17}$$

$$Z_j = cos(\alpha * j)\cdot\left(R + PEc_j\right) \tag{18}$$

$$Y_j = cin\ (\alpha * j)\cdot\left(R + PEc_j\right) \tag{19}$$

In practice, the compensation is implemented at the program level by updating the circular-path control points in the FANUC program. Specifically, the nominal point list defined by the N_1 control points (Y_j,Z_j) is replaced by a compensated point list computed using the averaged compensation error PEc_j (Eq. 17) and the corresponding coordinates in Eqs. 18–19. To obtain PEc_j, the dense ballbar samples are evenly partitioned into N_1 segments, and the mean error within each segment is assigned to the corresponding control point. In this way, each control point is corrected based on the locally measured deviation. The updated point list can then be exported as a corrected circular program and re-executed for validation. In the robot controller, the original circular program is updated by replacing the nominal control-point coordinates with the compensated ones in the same user frame and tool frame. Importantly, only the control-point coordinates are modified. This enables a controller-independent, offline workflow that can be executed with standard robot programming interfaces. Accordingly, Eq. 20 is introduced as a practical guideline for selecting the sampling rate and related experimental parameters.

To ensure consistency between ballbar measurement and actual machining, a practical constraint was established linking the sampling rate f_s, feed speed F (mm/min), number of control points $N1$, and circular path radius R_n(mm). The minimum required sampling rate is given by:

$$f_s \geq \frac{N1 \cdot F}{120\ \pi\ R_n} \tag{20}$$

This condition ensures at least one valid sample per control-point transition, avoiding aliasing between measurement and machining

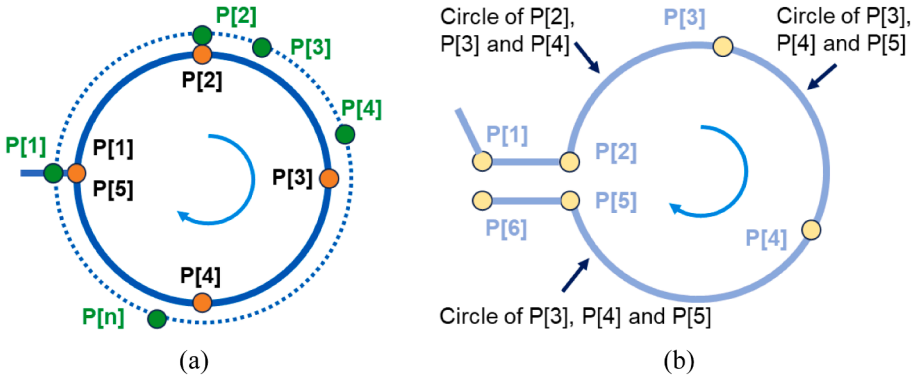

Fig. 6. Circular path generation method for hexapod: (a) Circular path generation using point to point method (green colour) and circular motion method (orange colour); (b) Circle arc motion command based continuous-path strategy for circular path generation, here is with five controlling points.

trajectories. In practice, a safety factor k ∈[2,5] is applied to increase robustness. Reference to this equation provides a practical guideline for selecting appropriate experimental parameters to ensure effective path error compensation.

Although this offline strategy requires an initial measurement, it improves efficiency compared with full robot calibration by focusing only on the local circular path.

3.2. Compensation comparison with laser tracker

A practical approach to evaluate circular path error measurement and compensation using a laser tracker, with comparative analysis against a ballbar, is to use both devices simultaneously. As illustrated in Fig. 7 (a), spherically mounted retroreflector (SMR) and the ballbar can be mounted together. For circular motion of the hexapod TCP, both measurement devices operate in two parallel YZ planes. Thus, to enable comparison, the laser tracker data must be translated to the ballbar's YZ plane. This requires knowledge of the offset between the SMR and the TCP. Among various methods, such as manual adjustment, offline calibration, or treating the offset as an unknown in the kinematic model, three-axis rotation of coordinate planes [21] offers a faster and more precise estimation of this offset, as well the transformation matrix between the laser tracker and hexapod base frames using Procrustes Analysis method [22].

To evaluate the circular path error, the following steps, illustrated in Fig. 7(b), are performed:

Step 1. The nominal circular path points P_f are generated by the hexapod controller in the hexapod reference frame $\mathcal{F}_b$.
Step 2. Because the error is assessed in the ballbar's ZY-plane for consistency, there with the known offset vector **u**between the hexapod flange and the TCP, the corresponding nominal TCP points P_t are computed.
Step 3. A 3D least-squares fitting is applied on P_t data to determine the optimized nominal circular path Γ_t, its center, and constant radius r_t.
Step 4. Simultaneously, the laser tracker records the SMR positions P_s. With the known offset vector **v** between the SMR and TCP, and the transformation matrix between the laser tracker and hexapod base frames, the measured TCP points $\widetilde{P}_t$ are obtained.
Step 5. A second 3D least-squares fitting is performed on $\widetilde{P}_t$ to determine the measured circular path $\widetilde{\Gamma}_t$, its center, and radius $\widetilde{r}_t$. To streamline machining-path error compensation and directly compare with ballbar results, we instead mount the SMR at the TCP. This removes the need for offset vector **v** and yields simply $\Gamma_s = \Gamma_t$.
Step 6. Finally, the circular path error is then calculated as the difference between the nominal and measured radii, r_t and $\widetilde{r}_t$.

3.3. Summary of compensation framework

Unlike the ballbar system, which only detects distance changes along its measurement axis, the laser tracker provides full 3D spatial coordinates of each control point along the circular trajectory. In this study, a 3D least-squares fitting algorithm was applied to the laser tracker data to determine the rotation center of the path and compute the true spatial radius at each sampled position. For comparative purposes, the radial deviation was then calculated as the difference between each point's fitted radius and the nominal path radius. To ensure a fair comparison with the ballbar-based method, the compensation was intentionally restricted to the YZ plane, excluding the X-axis component. This approach aligns the data usage and correction direction with those of the ballbar, allowing for a controlled evaluation of the proposed compensation scheme under equivalent conditions. The full 3D measurement capability of the laser tracker, however, remains available and is later used as a reference to assess whether the ballbar's directional limitations introduce significant error. A detailed comparison of the error evaluation and compensation capabilities across the ballbar, 2D-projected laser tracker, and full 3D laser tracker strategies is provided in Appendix C. This comparison outlines the dimensional scope, observability, and practical applicability of each method, and serves to clarify the rationale behind the compensation choices made in this study.

4. Experimental setup

Tests for circular path error compensation were performed on a hexapod machining cell comprising two Fanuc F200iB hexapods. The repeatability of the hexapods was ±0.1 mm. During ballbar measurements and milling operations, the hexapod mounted on the wall remained stationary, while the floor-mounted hexapod was rotated to generate circular motion. A Renishaw ballbar with nominal length of 50 mm and 100 mm was used (Fig. 9 (a to c)). The specifications of the ballbar were as follows: a measurement range of ±1 mm, a resolution of 0.1 μm, and a sampling rate of 1000 Hz. A custom-developed program ensured the maximum and constant sampling rate of 1000 Hz. For comparison of path error compensation using ballbar, a Faro ION laser tracker was also employed, featuring a resolution of 0.5 μm and an accuracy of 8.8 μm within a testing range of 2 m. During the robotic milling, the circular path error measured by the ballbar and laser tracker and their compensation values are used for tool path trajectory compensation.

For the robotic milling process, a 6061-T651-aluminum cylinder with a radius of 55 mm was employed (Fig. 9 (d)). The 6061-T651 aluminium is 6061 aluminium in the T651 temper. The NIAGARA SOLID CARBIDE A345-0.500-D3-S.0-Z3 cutter for aluminium alloy with a diameter of 12.7 mm was utilized. The specification of the workpiece

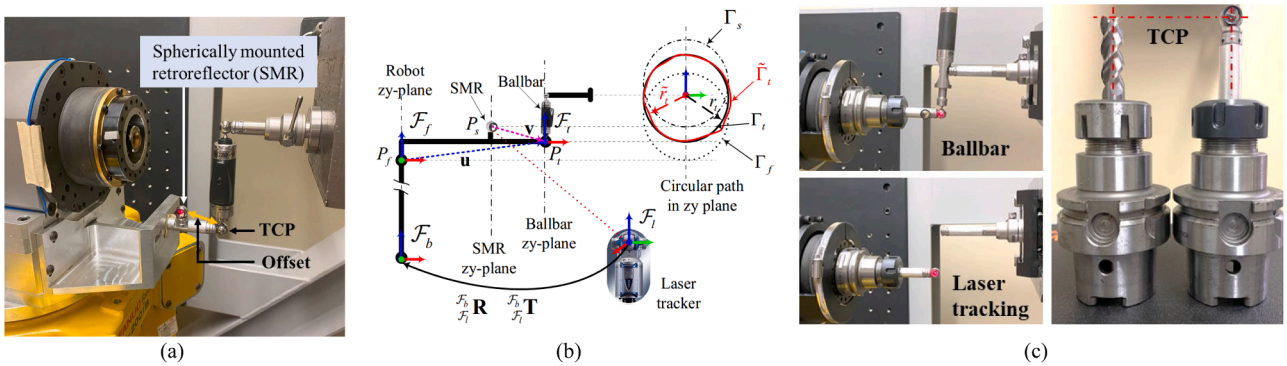

(a) (b) (c)

Fig. 7. Path error measurement using laser tracker: (a) Installation of the laser tracker SMR and the ballbar on hexapod robot; (b) Circular path error calculation process using laser tracker and ballbar, simultaneously; (c) Installation of ballbar and laser tracker on the circular path error measurement where the SMR is well matched with the TCP.

and cutter are shown at Table 1. The workpiece featured two circular profiles with diameter differences of 0.2 mm in the radial direction and 8 mm in the axial direction. These profiles were machined using both compensation and non-compensation operations. Due to the absence of a coolant system on the hexapod machining cell, a small radial cutting depth of 0.1 mm was selected. The other cutting parameters were as follows: a spindle speed of 10,000 RPM, an axial cutting depth of 8 mm, and a feed speed of 60 mm/min. Following the robotic milling process, the dimensional accuracy and circularity of the workpiece were measured using a Hexagon coordinate measurement machine (CMM) (Fig. 9 (e)), while the surface roughness was evaluated using a Mitutoyo 178-561-12A Surface Roughness Tester (Fig. 9 (f)). For each cylindrical profile, two circular measurements in the CW and CCW directions were performed using CMM and PolyWorks 2024 software.

Prior to conducting the ballbar measurement, the calibration of the ballbar equipped with the improved small circle adaptor and the ballbar equipped with the Renishaw-provided small circle adaptor was performed (Fig. 8). Several fixed distances between the scanning ball and center ball were selected for the calibration of the two adaptors. The calibration process was carried out as follows: 1) The ballbar, assembled with the Renishaw-provided small circle adaptor, was initially calibrated using the Renishaw-provided calibration pad; 2) The ballbar was then used to measure the fixed distance between the two balls; 3) The ballbar was reassembled with the improved small circle adaptor, and steps 1 and 2 were repeated; 4) Steps 1 to 3 were repeated for several distances between the two balls (10 randomly selected distances ranging from 49 to 51 mm). Finally, using Eq. 7, the assembly angle β (around 5°) was calculated through least squares fitting. Appendix B summarizes the regression fit and residual analysis confirming $\beta \approx 5^\circ$ with high repeatability, while Appendix D provides an additional robustness test showing that repeated dismount–remount cycles of the ISCA introduce less than ±7 μm variation.

Prior to robotic milling, the circular path error of the tool trajectory was measured using a ballbar. The ballbar was installed at varying out-of-plane angles to evaluate different radii. Radii ranging from 48 to 50 mm were measured using the original Renishaw provided small-radius adaptor, while the remaining radii from 48 to 35 mm were measured using a newly developed small-radius adaptor. Robotic machining was performed on two circular profiles (S1 and S2) with radius ranging from 50 mm to 35 mm, differing by 0.2 mm in radius (Fig. 9 (f)). The larger profile (S2) was machined without path error compensation, while the smaller profile (S1) was machined with path error compensation. This approach aimed to mitigate the impact of workpiece reinstallation errors on the fixture.

To validate the proposed methods, the ballbar measurement with the nominal lengths of 100 and 50 mm were conducted at the effective out-of-plane from 0 to 45 degrees with feeding speeds of 1200 mm/min. For each measurement radius, the ballbar test was performed three times. After each test at a specific radius, the spherically mounted retroreflector (SMR) was positioned at the connection point of the ballbar tip, and its position was recorded by the laser tracker during the same circular path movement. This procedure was also repeated twice. The arc-based circular path method was selected for circular path generation, as it provides more control points along the circular path and exhibits fewer variations in machining compared to the point-to-point method.

Table 1
Specification of the workpiece and cutter.

No.	6061-T651-aluminum		NIAGARA A345-0.500-D3-S.0-Z3 cutter	
1	Ultimate Tensile Strength (MPa)	320	Cutter diameter (mm)	12.7
2	Modulus of Elasticity (GPa)	69	Cutting edge count	3
3	Elongation (%)	11	Flute helix angle (degree)	45°
4	Hardness (HB)	90-105 HB	Overall length (mm)	76.2
5	Main alloying elements	AlMg1SiCu	Coating	None

5. Experimental results and analysis

5.1. Compensation effectiveness in non-machining tests

The ballbar, with a length of 50 mm, was tested with various out-of-plane angles ranging from 0° to 45°. Measurements of path radius at 48 mm, 49 mm, and 50 mm were conducted using both the improved small-circle adaptor and the Renishaw-provided small-circle adaptor. Additionally, to validate the effectiveness of the out-of-plane ballbar method for path error measurement and compensation, a laser tracker was employed immediately following the ballbar test using the setup described in Fig. 7. The ballbar and laser tracker are compared in terms of measured raw data, radial error curve pattern, circular deviation, and compensation rate. The measured raw data represents the deviation between the actual and nominal radius. The radial error curve pattern is commonly used to assess the geometric state of the machine tool, as key machine error parameters can be identified through its analysis [23]. Additionally, the radial error is derived from the measured raw data using the least-square fitting method to eliminate center offset [24]. Circular deviation indicates the variation range of the fitted ballbar raw data (radial error) [25]. To facilitate a comprehensive comparison of compensation effectiveness, a compensation rate is defined and calculated using the following equation:

$$Comp\_rate = \frac{CD_{before} - CD_{after}}{CD_{before}} \tag{21}$$

Fig. 10 reveals the change tendency of ballbar raw data measured with the Renishaw provided small circle adaptor (SCA) and the improved small circle adaptor (ISCA) at the radius of 48-, 49- and 50-mm. The ballbar raw data exhibits slight variations, with a maximum of 0.01 mm at certain angular positions at the CCW direction when using SCA and ISCA (Fig. 10 (a)). Similar results could be shown in the CW direction. This variation may result from thermal fluctuations in the experimental platform or minor rotation of the ISCA during ballbar measurement due to changes in friction between the scanning ball and the magnet cup. While as for the CD values (Fig. 10 (b)), SCA and ISCA have similar CD values, and their changes are matched with the change tendency of the ballbar raw data. From this, we can conclude that the ISCA and SCA have similar performance in the ballbar measurement using the standard length of 50 mm.

To further validate the performance of the out-of-plane ballbar method, tests are conducted using the ballbar with the ISCA at radius of 35, 40, 45, 48, 49, and 50 mm. For comparison, a laser tracker is also employed for circular path error measurement. The ballbar raw data measured by both methods before and after circular path error compensation are presented in Fig. 11. For ballbar measurements, the range of ballbar raw data decreases for each radius after circular path error compensation. However, the front section of the ballbar raw data for radius of 35 and 40 mm is larger than that for 45, 48, 49, and 50 mm, which may be attributed to the positioning error of the hexapod (Fig. 11 (a and b)). Similarly, for laser tracker measurements, the range of ballbar raw data also decreases after compensation (Fig. 11 (c and d)). Additionally, the raw data measured by laser tracker become more stable compared to those recorded before compensation. By comparing the results of the ballbar and laser tracker, it is observed that the range of ballbar raw data is generally larger than the one measured by the laser tracker. This discrepancy may be attributed to differences in the resolution of the two measurement devices or variations in data processing methods, as the ballbar employs least-square fitting for 2D data, whereas the laser tracker utilizes a 3D least-square fitting approach.

Regarding the radial error calculated using the measured raw data and the least-square fitting method, distinct radial error curve shapes are observed for the ballbar and laser tracker, as shown in Fig. 12. Similar variations are also present in the CW direction. For the ballbar,

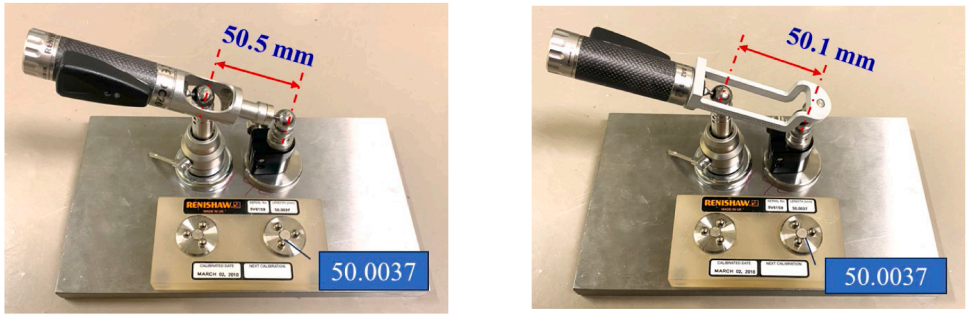

Fig. 8. Calibration of the improved small circle adaptor: (a) Measurement of the fixed distance between two balls using the Renishaw-provided small circle adaptor; (b) Measurement of the fixed distance between two balls using the improved small circle adaptor.

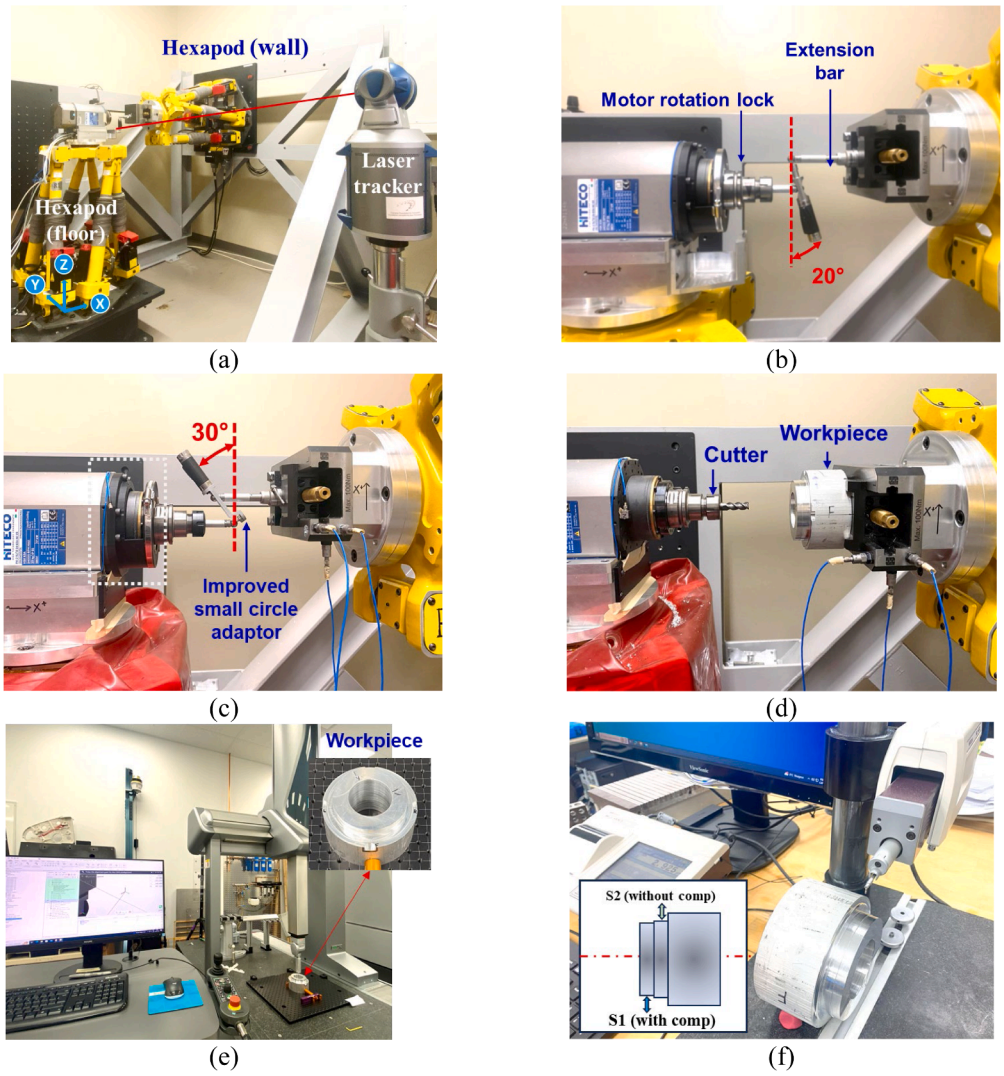

Fig. 9. Setup for out-of-plane ballbar measurement and its application for robotic milling: (a) circular path error measurement using ballbar and laser tracker; (b) Specialized fixture for the synchronization of data acquisition of ballbar and laser tracker in one measurement process; (c) Installation of ballbar with the length of 50 mm for the measurement of the circle with the radius of 47 mm; (d) Robotic milling of workpiece; (e) Measurement of dimension and circularity of workpiece using CMM; (f) Measurement of surface roughness using Mitutoyo Surface Roughness Tester.

significant changes in the radial error shape occur at angular positions of 0° and 180°. When the radius is smaller than 40 mm, the shape gradually transitions toward a full circle (Fig. 12 (a)). After circular path error compensation, the magnitude of the radial error decreases, while the primary curve shapes remain consistent (Fig. 12 (b)). For the laser tracker, similar radial error curve shapes are observed across different radii before compensation (Fig. 12 (c)). After compensation, a scaling effect in the radial error curve shape is evident, along with a reduction in radial error magnitude (Fig. 12 (d)).

Before circular path error compensation using ballbar, comparable

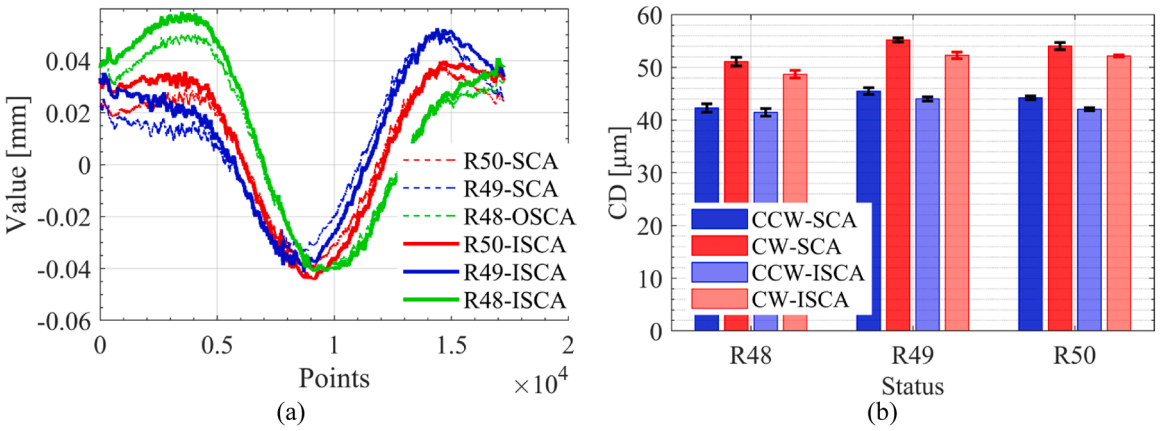

Fig. 10. Out-of-plane ballbar measurements performed at a radius of 48–50 mm using the SCA and ISCA setups, (a) Ballbar raw data measured with Renishaw provided small circle adaptor (SCA) and improved small circle adaptor (ISCA) on different path radius of 48, 49 and 50 mm at the CCW direction; (b) CDs measured with SCA and ISCA on different path radius of 48, 49 and 50 mm.

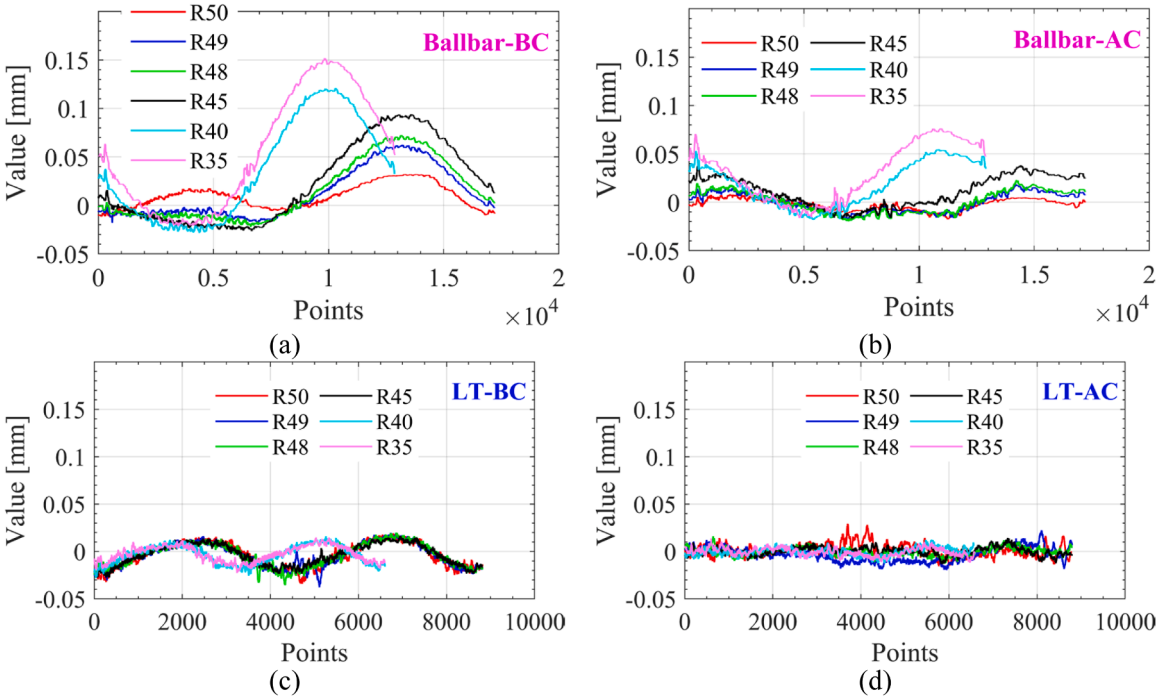

Fig. 11. Path error before and after compensation using ballbar and laser tracker (LT): (a) Circular CCW path error measured with a ballbar at different radii before error compensation (BC); (b) Circular CCW path error measured with a ballbar at different radii after path error compensation (AC); (c) Circular CCW path error measured with a laser tracker at different radii after path error compensation (LT-BC); (d) Circular CCW path error measured with a laser tracker at different radii after path error compensation (LT-AC).

CDs were measured across all testing radius, ranging from 42 μm to 50 μm (Fig. 13 (a)). However, after compensation, CDs exhibited varying degrees of reduction across different radiuses. The most effective compensation was observed at a radius close to 50 mm (out-of-plane angle of 0°), while the least effective compensation was found at a radius of 35 mm (out-of-plane angle of 45°). A similar trend was noted in the compensation rate, which increased with the ballbar radius and decreased as the ballbar out-of-plane angle increased. In addition, the maximum and minimum compensation rate could be found at 58% and 14% (Fig. 13 (b)), respectively. Consequently, it is concluded that the compensation effect of the circular path deteriorates as the radius decreases from 50 mm to 35 mm, corresponding to an increase in the out-of-plane angle from 0° to 45°, when utilizing the ISCA. By comparing the CDs after compensation, similar results were obtained for radius ranging from 45 mm to 50 mm (out-of-plane angle decreased from 30° to 0°), indicating improved compensation performance within this range.

For the laser tracker, prior to circular path error compensation, similar CDs were measured at radius of 48, 49, and 50 mm, while a decreasing trend in CDs was observed from 45 mm to 35 mm (Fig. 13 (c)). After compensation, CDs exhibited varying degrees of reduction across different radii, ultimately converging to a similar state. Effective compensation was achieved at most radii, except for an unexpected compensation result at a testing radius of 49 mm in the CCW direction, where the compensation rate was 18% (Fig. 13 (d)). For the remaining measurements, compensation rates ranged from 30% to 60%, indicating a generally effective compensation performance. Therefore, circular path error compensation using the laser tracker demonstrates satisfactory effectiveness across most tested radius.

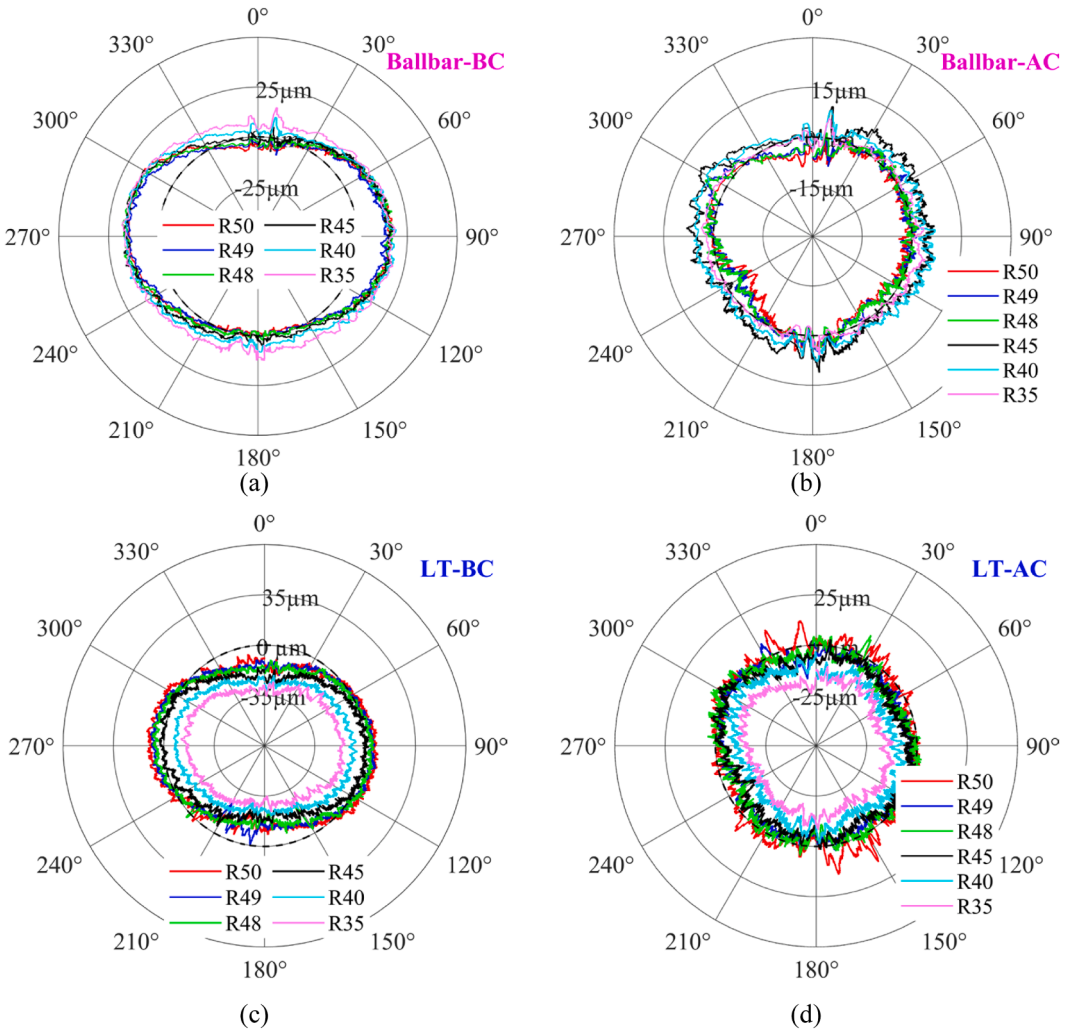

Fig. 12. Radial error measured by out-of-plane ballbar method using ballbar and laser tracker: (a) Radial error measured at the CCW direction before path error compensation using ballbar (Ballbar-BC); (b) Radial error measured at the CCW direction after path error compensation using ballbar (Ballbar-AC); (c) Radial error measured at the CCW direction before path error compensation using laser tracker (LT-BC); (d) Radial error measured at the CCW direction after path error compensation using laser tracker (LT-AC).

By analyzing the CDs and compensation rates obtained from measurements using the ballbar and laser tracker, effective compensation was observed for out-of-plane angles below 30°. The CDs were found to be approximately 22∼25 μm (with a compensation rate of 45∼60%) for the ballbar and 22∼35 μm (with a compensation rate of 20∼60%) for the laser tracker, indicating satisfactory performance for both measurement tools. Due to differences in least square fitting methods (2D for the ballbar and 3D for the laser tracker) and varying measurement resolutions, discrepancies in measurement and compensation results were observed. As the laser tracker is a standard tool for robot calibration and path error compensation, the ballbar, when used as a compensation tool, exhibited similar results. This confirms the effectiveness of the proposed out-of-plane ballbar method for circular path error measurement and compensation.

For broader context, a comparison with optical and laser-based metrology methods is summarized in Appendix F, highlighting that the proposed ballbar approach achieves compensation performance within the same order of magnitude at significantly lower cost and complexity.

5.2. Compensation effectiveness in actual machining

The aluminum workpiece has a nominal diameter of 50 mm and is machined using a milling tool with a radius of 6.35 mm. For the purpose of path error analysis, the tool center follows circular trajectories with radii ranging from 35 mm to 50 mm for two profiles (S1 and S2) milling. The two profiles vary with an increment of 0.2 mm. The smaller circular profile (S1) is machined with path error compensation (ballbar or laser tracker), whereas the larger circular profile (S2) is machined without path error compensation. Since the locations of the two profiles are very close, the compensation and non-compensation effect on the circular path error can be well compared with minimalization of the reinstallation error of the workpiece on the robot and CMM. In contrast to the non-machining compensation discussed previously, the machining-based circular-path error compensation uses a setup in which the SMR is mounted directly at the TCP (Fig. 7 (c)). This eliminates any TCP–SMR offset calculations and allows both the SMR and the ballbar to move in the same plane.

A typical example of a machining operation is illustrated in Fig. 14, which presents the ballbar raw data and the radial error of a circular path with the tool center path radius of 49.4 mm before and after circular path error compensation in both non-machining and machining states. In the non-machining state, the variation range of the ballbar raw data is reduced following circular path error compensation. Additionally, the mean value of the ballbar raw data decreases from 0.03 mm to 0.01 mm (Fig. 14 (a)), contributing to the stabilization of the final

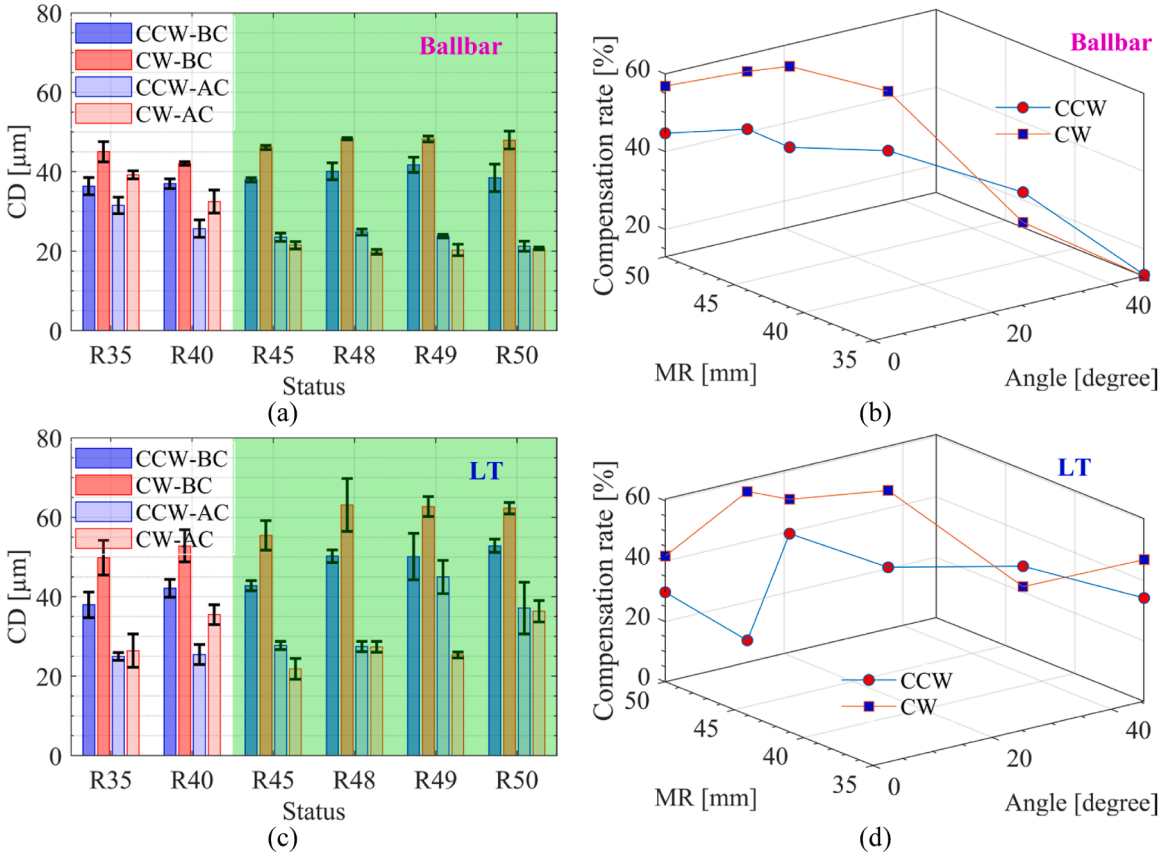

Fig. 13. CDs and compensation rate of out-of-plane ballbar and laser tracker measurements. (a) CDs measured with ballbar before (BC) and after (AC) compensation; (b) Compensation rates of the ballbar as a function of out-of-plane angle and measured radius (MR); (c) CDs measured with laser tracker before (BC) and after (AC) compensation; (d) Compensation rates of the laser tracker as a function of out-of-plane angle and MR.

dimensions of the machined part. Regarding radial errors, prior to compensation, the variation range is within ±45 μm, and a clear scaling mismatch error is observed on the ballbar measurement plane (Fig. 14 (b)). However, after compensation, a significant reduction in the radial error variation range is achieved, and the scaling mismatch error is eliminated (Fig. 14 (c)). Based on the calculated circular path error compensation values, the machining program for circular path milling is updated accordingly. For the workpiece, in a single installation, after conducting ballbar measurements in the non-machining state, surfaces S1 and S2 are milled with and without circular path error compensation. Following machining, the circularity and surface roughness of both surfaces are evaluated using a CMM and a Surface Roughness Tester. A comparison of the CMM raw data (profile error of the workpiece) for both surfaces reveal a significant reduction in profile error variation after circular path error compensation (Fig. 14 (d)). Furthermore, the scaling mismatch error reflected on the workpiece is also reduced from ± 30 into ± 10 μm, leading to improved circularity in the final milling process (Fig. 14 (e, f)). Regarding circular deviation and circularity, after circular path error compensation, the circular deviation is reduced from 43 μm to 14 μm, while circularity decreases from 43 μm to 13 μm. Since the cutting depth in profile milling is minimal, the positioning error of the hexapod becomes the dominant factor influencing the workpiece tolerance. This explains the observed similarity between the circular deviation and circularity. For the remaining machining tasks involving workpieces with tool center path radius ranging from 35 to 50 mm, the circular deviation and circularity exhibit a similar trend to those observed for the 49.4 mm radius. Although the compensated errors in (Fig. 14 (a, d)). exhibit a slight negative bias, this does not compromise machining quality, as both circularity and dimensional stability were significantly improved. If necessary, the bias can be eliminated through a trivial offset correction in subsequent iterations.

To better compare machining quality, circularity, circularity compensation rate (hereinafter referred to as compensation rate), and surface roughness parameters Ra and Rz, and the variation of measured workpiece dimension and relative improvement rate are analyzed. Ideally, smaller values of circularity, Ra, and Rz, along with a higher compensation rate, are preferred after circular path error compensation. Fig. 15 illustrates the variation in these parameters for circular profile milling within the tool center path radius range of 35 to 50 mm. To enhance the presentation of machining results, the ballbar-equivalent tool center path radius for profile S2 is shown, as a negative radial difference of 0.2 mm exists at S1. As the workpiece radius decreases, the circularity without compensation is reduced from a maximum of 43 μm to 38 μm, while the circularity with compensation increases from 13 μm to 25 μm (Fig. 15 (a)). Simultaneously, the compensation rate declines from a maximum of 67% to 25% (Fig. 15 (b)). It is observed that under the ballbar angle setup, the effectiveness of circular path error compensation decreases. However, when the out-of-plane angle exceeds 30°, a higher compensation rate of over 40% is achieved. The results of ballbar circular path error compensation align with the findings from ballbar tests in the non-machining state. Specifically, a smaller out-of-plane angle yields a more effective compensation effect. Regarding the surface roughness parameters Ra and Rz (Fig. 15 (c, d)), similar results are observed for each circular milling operation. Under identical cutting parameters, circular path error compensation does not significantly affect machining quality in terms of surface roughness. The variation in the measured workpiece dimension and relative improvement rate reflects the effectiveness of the compensation on the final workpiece dimension, which directly affects the tolerance level when within a reasonable and acceptable range. The relative improvement rate is

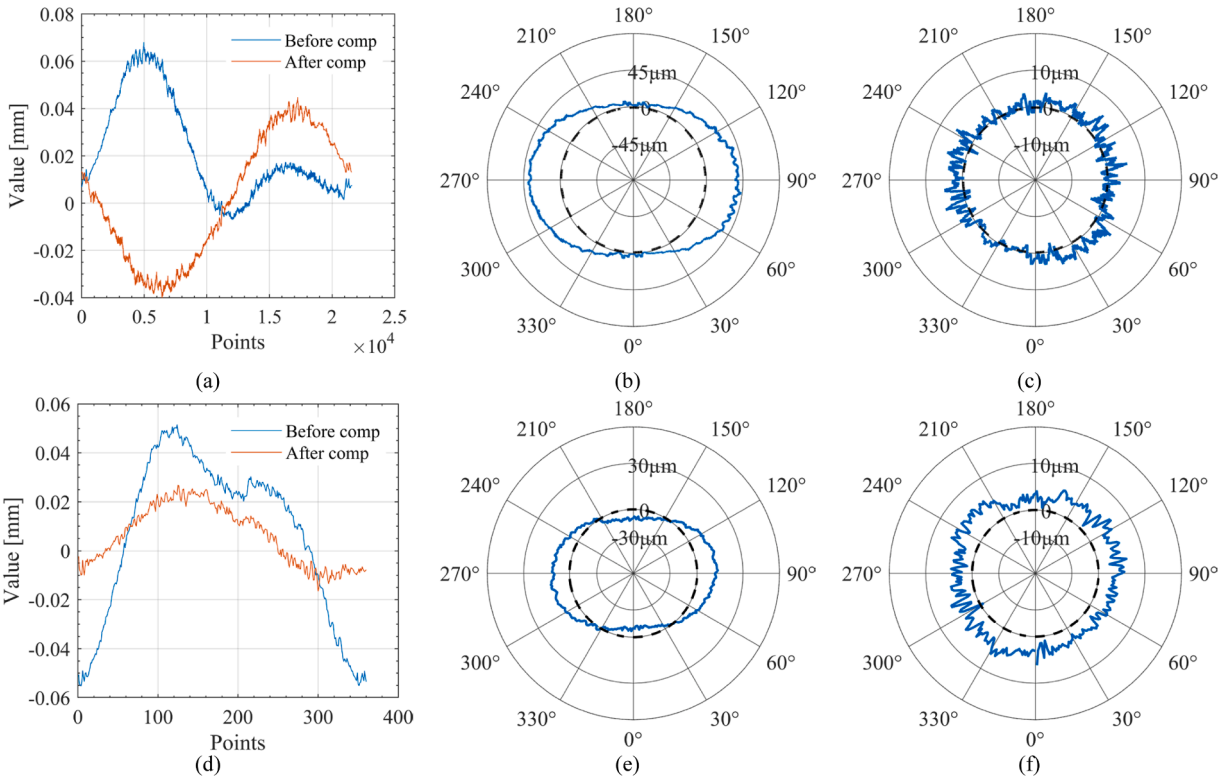

Fig. 14. Comparison of radial and profile errors before and after circular path error compensation using ballbar and laser tracker. (a–c) Radial errors of a 49.4 mm tool center path radius in the non-machining state: (a) Raw measurement results before and after compensation using ballbar; (b) Radial error trajectory without compensation;(c) Radial error trajectory with compensation. (d–f) Profile errors of the workpiece in the machining state: (d) Overall profile deviation before and after compensation using laser tracker; (e) Profile error curve without compensation; (f) Profile error curve with compensation.

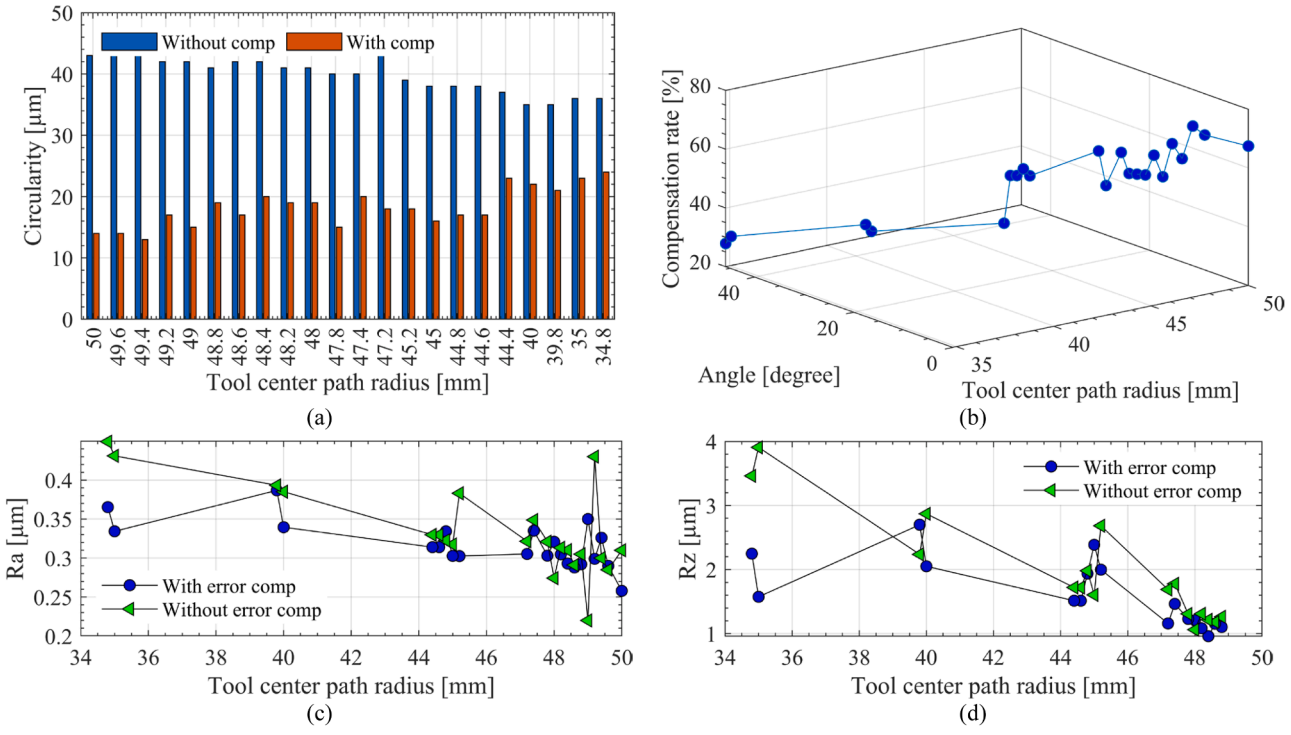

Fig. 15. Machining quality comparison: (a) Circularity of the workpiece machined with and without circular path error compensation, measured using a ballbar; (b) Relationship between the workpiece radius (tool center path radius), ballbar out-of-plane angle, and compensation rate under circular path error compensation; (c) Surface roughness (Ra) of the workpiece machined with and without circular path error compensation; (d) Surface roughness (Rz) of the workpiece machined with and without circular path error compensation.

defined as the ratio of the reduction in dimensional variation due to error compensation to the original variation without compensation. Ideally, a minimized variation and a higher relative improvement rate are expected to be minimized. Fig. 16 (a) reveals the variation range and relative improvement rate of the measured workpiece dimension with and without circular path error compensation using the proposed ballbar-based method. For the machining tasks, the variation in the measured workpiece dimensions ranged from 0.098 mm to 0.120 mm. After circular path error compensation, the variation was reduced to a range of 0.035 mm to 0.066 mm, resulting in a relative improvement rate between 35.90 % and 62.99 %. Additionally, the lowest relative compensation rates were observed at smaller workpiece dimensions, indicating the effective compensation range of the proposed ballbar installation method.

Although circular path error compensation is effective, the reason for the lower compensation rate at out-of-plane angles between 30° and 45° remains difficult to define. One possible explanation is that as the out-of-plane angle increases, the ballbar can only capture partial information along its measurement surface, while unexpected movements along the axis perpendicular to this surface may occur, reducing the effectiveness of compensation. This hypothesis can be verified using a laser tracker. Under identical cutting parameters, circular milling is also compensated with a laser tracker, allowing for validation and comparison of both methods.

5.3. Comparative analysis: Ballbar vs laser tracker on part machining

Fig. 16 presents the variation range and relative improvement rate of the measured workpiece dimensions with and without circular path error compensation using the proposed ballbar-based method (a) and the laser tracker-based method (b). For machining tasks involving workpieces with tool center path radius ranging from 35.2 mm to 47.6 mm, the variation in the measured dimensions prior to compensation with the laser tracker ranged from 0.078 mm to 0.118 mm. After circular path error compensation, the variation was reduced to a range of 0.042 mm to 0.052 mm, resulting in a relative improvement rate between 40.1 % and 56.8 %. Similarly, for the ballbar-based method (Fig. 16 (a)), applied to workpieces with tool center path radius from 34.8 mm to 47.8 mm, the variation in the measured dimensions ranged from 0.081 mm to 0.119 mm before compensation. Following compensation, the variation was reduced to a range of 0.039 mm to 0.066 mm, yielding a relative improvement rate between 35.4 % and 54.3 %. A comparison between the ballbar-based and laser tracker-based methods indicates comparable compensation effectiveness in the improvement of circular part machining.

Fig. 17 reveals a comparison between ballbar and laser tracker measurements for milling workpieces with tool center path radius ranging from 34.8 mm to 47.8 mm. For specific workpiece radius, path error compensation using a laser tracker was incorporated into the tests where ballbar-based compensation was also performed. For each main radius at around of 35, 40, 45 and 47 mm, ballbar and laser tracker measurements are conducted sequentially. After circular path error compensation, the circularity of each circular profile milling significantly decreases. The decrease amount of circular deviation ranging from 12 to 25 μm with the ballbar and from 8 to 22 μm with the laser tracker could be found, respectively (Fig. 17 (a)). Additionally, for the main radius around 35, 40, 45, and 47 mm, no significant difference in circularity is observed before and after compensation using either method. This trend is also reflected in the compensation rate parameter, despite minor variations (Fig. 17 (b)). Furthermore, similar distributions of Ra and Rz are observed when applying ballbar and laser tracker compensation, though a slight improvement in surface roughness is noted (Fig. 17 (c, d)).

By comparing the above results, it is evident that the proposed out-of-plane ballbar method effectively measures radial errors at arbitrary radius, and the corresponding path error compensation strategy is successful. At a small out-of-plane angle, circular path error compensation yields reliable results, enabling the robotic machining platform to achieve high machining quality without requiring full robot calibration. To further verify that the compensated circular trajectories remained planar during machining, X-direction deviations were extracted from laser tracker measurements. As summarized in Appendix E, the deviations stayed within ±0.05 mm, confirming that the tested circular paths were essentially planar under the experimental conditions.

6. Discussion

Although the proposed out-of-plane ballbar configuration can, in principle, be applied to other motion platforms, the contribution of this work is primarily motivated by robotic machining and its deployment constraints. Compared with machine tools, industrial robots typically exhibit lower structural stiffness, stronger pose-dependent compliance, and more pronounced path deviations under process loads, while shop-floor integration often requires short downtime and minimal external instrumentation. In this context, the proposed approach is not presented as a generic circular test, but as a task-oriented, program-level trajectory

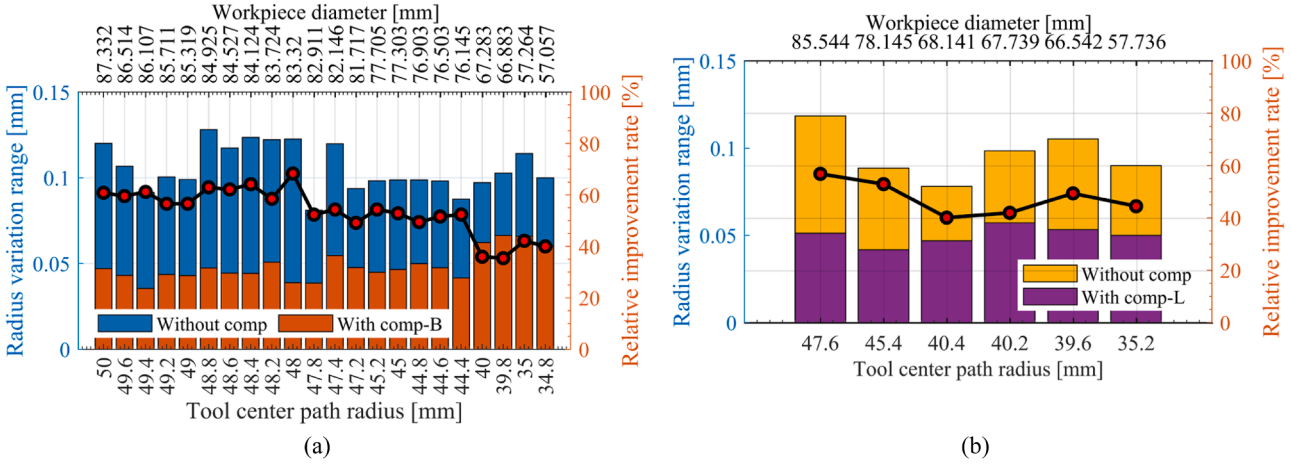

Fig. 16. Workpiece machining quality under path error compensation with ballbar and laser tracker: (a) Variation range and relative improvement rate of the measured workpiece dimensions machined along tool center path radii, with and without circular path error compensation using the proposed ballbar-based method; (b) Variation range and relative improvement rate of the measured workpiece dimensions machined along tool center path radii, with and without circular path error compensation using the laser tracker-based method.

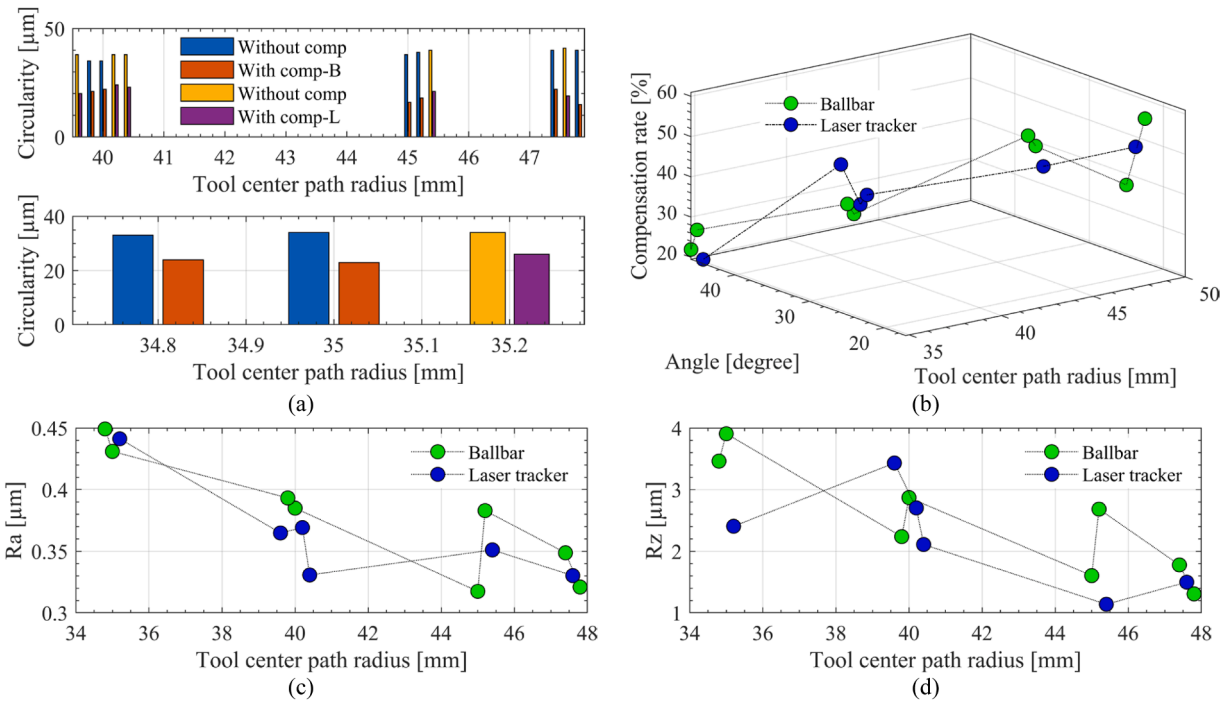

Fig. 17. Comparison of workpiece machining quality under circular path error compensation with ballbar and laser tracker: (a) Circularity of the machined workpiece machined along tool center path radii, with and without circular path error compensation by using a ballbar (B) and a laser tracker (L), respectively; (b) Relationship among the tool center path radius, ballbar out-of-plane angle, and compensation rate under circular path error compensation, evaluated using a ballbar and a laser tracker, respectively; (c) Surface roughness (Ra) of the machined workpiece with circular path error compensation, measured using a ballbar and a laser tracker, respectively; (d) Surface roughness (Rz) of the machined workpiece with circular path error compensation, measured using a ballbar and a laser tracker, respectively.

compensation method that converts high-resolution ballbar measurements into corrections directly applied to the circular-arc control points of the robotic machining program. The method therefore targets a practical workflow in which the same robot, tool, and cell can be rapidly verified and compensated without requiring full volumetric calibration or complex optical setups. The machining-oriented validation results further demonstrate that the proposed compensation is effective in improving circular-path accuracy under realistic robotic machining conditions, which is a key distinction from diagnostic-only circular tests commonly used in other domains.

The present study focuses on circular trajectories with radii of 35–50 mm because small-radius circular features are frequently encountered in robotic machining and they also represent a regime in which conventional ballbar systems are constrained by discrete nominal diameters. For large-scale robotic applications, optical metrology systems such as laser trackers or photogrammetry can be advantageous due to their large working volume. However, as mentioned in the introduction, there are practical limitations in the use of these devices. In this sense, the proposed out-of-plane ballbar approach is intended as a complementary solution that provides high sensor resolution and rapid deployment for circular-path verification and program-level compensation. Regarding scalability, the same framework can be extended to larger radii by using longer ballbars and extension bars, while maintaining the same error-to-control-point mapping and program update procedure. For very large structures, the method can be applied in a segment-wise manner to compensate representative circular features or local circular arcs along the process path.

A novel ballbar angular setup method for circular path error compensation has been introduced and validated in this study, addressing the limitations associated with conventional fixed-radius ballbar measurements. Through the development of a customized small-circle adaptor (ISCA) and the extension of the angular setup range, the proposed method enables effective characterization and compensation of circular trajectory errors for radii between 35 mm and 50 mm. The ISCA design and calibration have been validated through regression analysis of the assembly angle β (Appendix B) and robustness tests under repeated dismount–remount cycles (Appendix D), confirming stable performance with less than ±7 μm variation. Improvements in circular deviation (CD) following compensation, particularly at out-of-plane angles below 30°, demonstrate the method's efficacy under both non-machining conditions and actual milling processes. When compared with high-end laser tracker-based systems, the proposed approach provides a practical and cost-effective alternative, delivering comparable compensation performance within a constrained yet industrially relevant operational range.

Machining validation conducted on cylindrical parts, both with and without compensation, confirmed significant enhancements in circularity and dimensional stability, while surface roughness parameters (Ra and Rz) remained consistent. These outcomes indicate that the method can be directly deployed in production environments requiring flexible and accurate machining of circular features. The method is particularly suitable for flexible manufacturing platforms where components of varying geometries must be machined without reconfiguring the metrology setup. Relevant applications include the precision machining of aerospace parts, medical implants, and high-performance mechanical couplings, where stringent tolerances are required but the use of laser trackers may be impractical due to cost or environmental constraints. Owing to its low setup complexity and calibration-free implementation, the method is also well-suited for robotic cells and compact multi-axis systems. In comparison to conventional CNC lathes or milling machines used for machining similar cylindrical features, the ballbar-compensated robotic setup offers notable advantages. While traditional machine tools achieve high accuracy through rigid kinematic structures and mature control systems, their adaptability to complex trajectories or varying part geometries is inherently limited. Conversely, a dual-robot system equipped with ballbar-based path error

compensation has been shown to achieve comparable geometric accuracy while providing enhanced flexibility for custom parts, small-batch production, and prototyping. The observed improvements in circularity during machining trials confirm that, with appropriate compensation, robotic platforms can narrow the precision gap traditionally separating industrial robots from conventional machine tools-particularly near the upper range of the tested diameters. It is also worth noting that the residual errors observed after compensation in Fig. 14 were predominantly negative, corresponding to a slight undershoot of the nominal radius. This bias did not compromise machining quality, since circularity and dimensional stability were markedly improved, and it can be readily eliminated through a trivial gain or offset adjustment in subsequent compensation iterations. In terms of novelty, the proposed method introduces four main contributions beyond existing optical or laser tracker approaches: (1) a generalized visibility model that quantifies measurable and blind components under out-of-plane configurations; (2) an improved adaptor enabling small-radius measurements down to 35 mm, extending the traditional 47–50 mm limit (Appendix A); (3) experimentally demonstrated compensation rates of 40–67% for out-of-plane angles up to 30°, which are comparable to laser tracker performance at a fraction of the cost (Appendix G), and positioning ballbar-based measurement against optical metrology (laser tracker and photogrammetry) from a shop-floor deployment perspective, clarifying typical accuracy levels and practical limitations (Appendix G). These advances collectively distinguish the present work from earlier studies relying solely on high-cost laser trackers or photogrammetry systems. For broader context, a comparison with representative optical and laser-based metrology systems is summarized in Appendix G, highlighting trade-offs in cost, accuracy, and deployment complexity.

A further distinction can be drawn between offline and online path error compensation strategies. The proposed method operates as an offline approach, wherein errors are measured in advance and manually integrated into the robot's motion program. This strategy offers low implementation cost, high repeatability, and straightforward integration, as it does not rely on real-time feedback or closed-loop control. Additionally, it remains robust against environmental disturbances once compensation parameters have been established. In contrast, online compensation approaches that employ real-time feedback from encoders, vision systems, or external sensors such as laser trackers allow dynamic error correction during machining. Although capable of addressing thermal drift, vibration, and tool deflection in real time, online systems impose higher computational demands and require complex hardware-software integration, potentially introducing control delays or instabilities during rapid or discontinuous toolpaths. Therefore, for applications where moderate accuracy, cost-efficiency, and ease of deployment are prioritized, the ballbar angular setup method provides a compelling alternative. By modifying toolpaths based on pre-characterized error patterns, it avoids the intricacies of closed-loop control while achieving adequate precision for a broad spectrum of industrial tasks. Beyond the tested hexapod platform, the proposed method was also validated on a six-DOF serial industrial robot (Appendix F). The serial-robot experiments show stable compensation trends and compensation rates within approximately 10–15% of the hexapod results, confirming that the proposed workflow is transferable across robot architectures with different stiffness and kinematic properties. Moreover, the offline compensation strategy demonstrated here could serve as a foundation for predictive control frameworks and online error compensation modules available in commercial systems, such as FANUC Dynamic Path Modification (DPM), ABB Externally Guided Motion (EGM), and KUKA Robot Sensor Interface (RSI). Integration with such real-time interfaces represents a promising avenue for future research. Looking forward, the proposed method could be extended into a ‘measure once, compensate many times’ workflow for batch machining scenarios. Although not implemented in the present study, this represents a promising avenue for improving efficiency in industrial applications.

Beyond geometric error reduction, the proposed method contributes directly to the robotic machining context. By lowering quasi-static deviations caused by compliance and assembly imperfections, the compensated trajectories establish a more favorable baseline for robot controllers, thereby reducing the magnitude of residual dynamic errors. Importantly, comparable compensation performance has been validated on both a parallel hexapod and a serial FANUC manipulator, confirming transferability across architectures with different stiffness and kinematic properties. Moreover, since the compensation is embedded at the trajectory level, it can be seamlessly integrated with existing robot control interfaces (e.g., FANUC DPM, ABB EGM, KUKA RSI). In this sense, the method is not merely a geometric correction but a robot-aware feedforward enhancement that leverages available industrial compensation frameworks.

In addition to radial in-plane errors, potential out-of-plane deviations were also examined. Laser tracker measurements confirmed that X-direction variations during machining were consistently below ±0.05 mm (Appendix E), which are smaller or comparable to the in-plane errors. Thus, under the tested conditions, the circular trajectories can be regarded as essentially planar. Nevertheless, such small out-of-plane deviations may still contribute to residual errors that remain invisible to the ballbar, which motivates future integration of full 3D metrology into the compensation strategy.

Nevertheless, certain limitations persist. At out-of-plane angles exceeding 30°, the undetectable component projected onto the blind direction increases and the effectiveness of compensation diminishes due to increased theoretical and axial motion errors. Additionally, for small-radius paths below 40 mm, both ballbar and laser tracker-based methods exhibit reduced compensation accuracy. These limitations may be addressed through mechanical enhancements, such as extension bar systems for larger radii, and by refining data fitting algorithms through advanced modeling techniques.

Although the present study focuses on circular path error compensation for diameters up to 50 mm, the proposed ballbar angular setup method is theoretically applicable to larger diameters, such as from 50 mm to 300 mm. Given the stability of the compensation trend observed within the tested range, along with the mechanical adaptability of the setup, comparable compensation performance is anticipated for larger circular profiles, provided that appropriate adaptors or extension bars are employed. Future work will experimentally validate the method across an extended diameter range. In addition, this study focuses primarily on analyzing the variation of toolpath radius before and after circular path error compensation, rather than the final dimensional accuracy of the machined parts. This approach aims to isolate the geometric effect of the compensation strategy itself, without interference from process-induced factors such as thermal deformation or tool wear. By quantifying changes in the effective radius, a more consistent and direct evaluation of compensation performance is achieved. This focus also facilitates comparison with high-precision metrology systems where trajectory-level accuracy is critical. Although part accuracy was recorded to ensure machining relevance, the core objective remains the assessment of how compensation influences the commanded toolpath geometry.

Finally, the proposed ballbar angular setup method extends the functional scope of conventional ballbar systems, enabling accurate and flexible error compensation in robotic machining contexts. Its low-cost, offline nature renders it an accessible solution for precision improvement in small- and medium-scale manufacturing operations. While not a replacement for high-end real-time metrology systems, its practical utility is evident in resource-constrained or geometrically variable production settings.

7. Conclusion and future work

This study explores the optimization of robotic machining through circular path error compensation. A novel out-of-plane ballbar method,

combined with an improved small circle adaptor and a corresponding data processing approach, is proposed for circular path error measurement within the 35~150 mm range. Theoretical analysis and experimental validation, conducted in both machining and non-machining states using ballbar and a laser tracker, confirm the method's effectiveness for variable-radius measurements and path error compensation.

1) The proposed out-of-plane ballbar method expands the applicability of traditional ballbar measurement from machine tool or robot accuracy measurement into path error measurement compensation and it extends the circular path error measurement range for non-uniform testing radius. However, its compensation rate decreases as the out-of-plane angle increases. For out-of-plane angles below 30°, the compensation rate ranging from 40% to 67% can be achieved under non machining state.
2) The proposed out-of-plane ballbar method demonstrates performance comparable to the laser tracker in circular path error measurement and compensation under machining conditions. Within the recommended setup angle range, machining profile circularity is effectively compensated, achieving a circularity compensation rate exceeding 40%. For other out-of-plane angles, the ballbar still maintains circularity similar to that of the laser tracker. Both methods yield comparable surface roughness in Ra and Rz across all machining operations. In addition, the proposed ballbar angular setup method exhibits comparable performance to the laser tracker in reducing the variation in the measured workpiece dimensions.

Due to the limitations of the current ballbar structure, the compensation rate of the ballbar angular setup method still has room for improvement. Further enhancements can be achieved through structural optimization of the ballbar and its calibration pad. Additionally, this study highlights the potential of integrating the proposed ballbar angular setup with online path error compensation for high-precision robotic machining. Building on this perspective, future research will extend the method toward a hybrid framework that couples offline ballbar-based geometric compensation with online modules available in industrial robot controllers. This combination will enable simultaneous mitigation of geometric and dynamic errors, integrating the high-resolution, low-cost advantages of the ballbar with the real-time adaptability of robot control interfaces such as FANUC DPM, ABB EGM, and KUKA RSI. Such integration will further strengthen the relevance of the proposed method to robotic machining scenarios, broaden its applicability across robot architectures with different stiffness and kinematic structures, and pave the way for predictive control strategies that unify measurement, compensation, and process optimization.

CRediT authorship contribution statement

Kanglin Xing: Writing – original draft, Visualization, Validation, Methodology, Investigation, Formal analysis, Data curation, Conceptualization. **J.R.R. Mayer:** Writing – review & editing, Resources, Methodology, Formal analysis, Conceptualization. **Yannick Cianyi:** Writing – review & editing, Validation, Resources, Investigation, Formal analysis. **Ilian A. Bonev:** Writing – review & editing, Supervision, Resources, Project administration, Funding acquisition, Conceptualization. **Zhaoheng Liu:** Writing – review & editing, Supervision, Resources, Funding acquisition, Formal analysis, Conceptualization. **Henri Champliaud:** Writing – review & editing, Validation, Supervision, Resources, Funding acquisition, Formal analysis.

Declaration of competing interest

The authors declare that they have no known competing financial interests or personal relationships that could have appeared to influence the work reported in this paper.

Acknowledgements

The authors gratefully acknowledge the financial support provided by the Fonds de recherche du Québec-Nature et technologies (FRQNT) through a postdoctoral research scholarship and the Natural Sciences and Engineering Research Council of Canada (NSERC). The authors also extend their gratitude to Mr. Joël Grignon, Dr. Xavier Rimpault, and Mr. Anthony Remington for their invaluable technical assistance with cutting parameter selection, CMM measurements, and the design and machining of the new small circle adaptor. Special thanks are offered to Mr. Guy Gironne, a retired technician from Polytechnique Montréal, for his preparation of the aluminum part and for providing training on the simulation of CNC machining.

Appendix A. Design of the Improved Small-Circle Adaptor (ISCA)

To supplement Section 2.1, the detailed design of the ISCA is provided in Fig. A (a–b). The ISCA was specifically developed to extend the measurement range of the QC20-W ballbar down to a 35 mm radius, thereby addressing the limitation of the commercial adaptor that only supports radii of 47-50 mm. Its design ensures reliable coupling, high repeatability, and sufficient stiffness for robotic machining error compensation.

As illustrated in Fig. A (a), the ISCA bridges the QC20-W ballbar and the pivot assembly (ISCA) via threaded interfaces. One end of the adaptor terminates in an M18 threaded joint, which secures the scanning ball of the QC20-W system. The opposite end incorporates an M6 threaded connection to mate with the center ball. This arrangement not only guarantees firm mounting but also allows for quick assembly and disassembly during repeated testing cycles. To reduce handling error, a locating shoulder is integrated into the ISCA side, providing self-centering and alignment robustness.

The engineering drawing in Fig. A (b) defines the critical dimensions and tolerances. The key length for the M6 is 68.5 ± 0.03 mm, with a critical positioning length of 20 ± 0.02 mm for M18 to ensure accurate spacing (around 50 mm) during circular path measurement. Threaded connections are specified as M6 × 1-6H and M18 × 1.5-6H. Geometric tolerances are applied to ensure stability: The M6 threaded hole is controlled by a positional tolerance of 0.05 mm relative to the mounting plane (datum A) and the M18 axis (datum B); The flatness of the mounting plane is specified within 0.01 mm to guarantee stable contact with the reference surface; The perpendicularity of the M18 threaded axis relative to datum A is limited to 0.012 mm, minimizing angular misalignment; Radii are controlled where necessary (R2 for unspecified edges, explicit R4 and R5 for fillets), reducing stress concentration while avoiding unnecessary over-constraint.

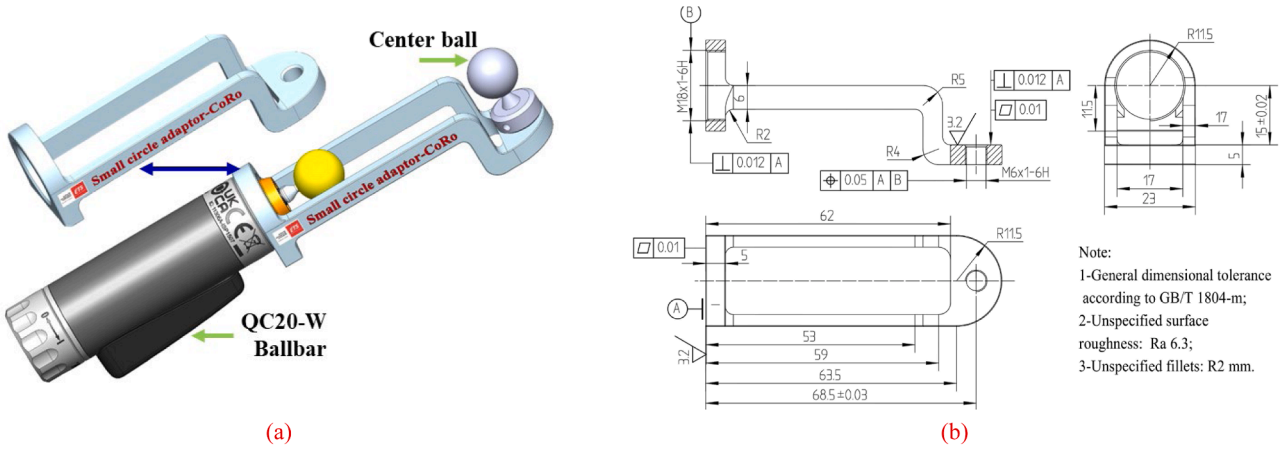

Fig. A. Improved small-circle adaptor (ISCA): (a) structural configuration assembled with the QC20-W ballbar; (b) engineering drawing showing key dimensions, tolerances, and technical notes.

The ISCA is fabricated from 6061-T651 aluminum, selected for its balance of machinability, stiffness, and weight. Anodizing is applied to enhance surface hardness and durability, preventing galling at the threaded interfaces during repeated tightening and loosening. The combined application of dimensional and geometric tolerances ensures that the ISCA maintains accurate positioning under repeated use. The dual-threaded design allows flexible attachment while avoiding cumulative misalignment. By constraining both the flatness of the mounting plane and the positional accuracy of the M6 thread, the adaptor minimizes systematic setup errors, which is essential for high-precision ballbar measurements. In summary, the ISCA integrates compact geometry, standardized threads, controlled tolerances, and anodized aluminium construction. These design choices collectively ensure mechanical stability, high repeatability, and ease of deployment, making the adaptor suitable for prolonged ballbar-based robotic trajectory measurement and compensation experiments.

Appendix B. Calibration of the assembly angle β

To ensure accurate compensation, the assembly angle β of the ISCA was experimentally calibrated against the Renishaw-provided reference adaptor (SCA). Ten paired measurements were acquired between the two balls with both adaptor readings constrained to 49-51 mm. For each fixed distance Di, the reference adaptor (β≈0°) produced y_i and the ISCA produced x_i. Because both adaptors measure the same true distance (common origin), calibration employs a through-origin model $y = bx$ with $b = cos\beta$ (see Fig. B (a) for the paired data and fitted line).). The estimator and confidence construction are:

$$\widehat{b} = \frac{\sum_i x_i\, y_i}{\sum_i x_i^2} \tag{B1}$$

$$s^2 = \frac{\sum (y_i - \widehat{b}x_i)^2}{n-1} \tag{B2}$$

$$SE(\widehat{b}) = \sqrt{\frac{s^2}{\sum x_i^2}} \tag{B3}$$

$$b_U = \widehat{b} + t_{0.975,n-1} \cdot SE(\widehat{b}) \tag{B4}$$

$$b_L = \widehat{b} - t_{0.975,n-1} \cdot SE(\widehat{b}) \tag{B5}$$

$$\widehat{\beta} = arccos\ (\widehat{b}) \tag{B6}$$

$$\frac{d\beta}{db} = -\frac{1}{\sqrt{1-b^2}} \tag{B7}$$

The through-origin fit gives $\widehat{b}$=0.99626 (95% CI [0.9960567, 0.9964654]), corresponding to β=4.9562° with 95% CI [4.9197°,4.9924°]. Residual scatter is low (RMSE = 0.0065 mm), and residuals show no visible trend over the 49-51 mm range (Fig. B (b)). This calibrated angle is consistent with the ≈5° design stated in the main text and is used for the compensation results and the fitted line shown in Fig. 8.

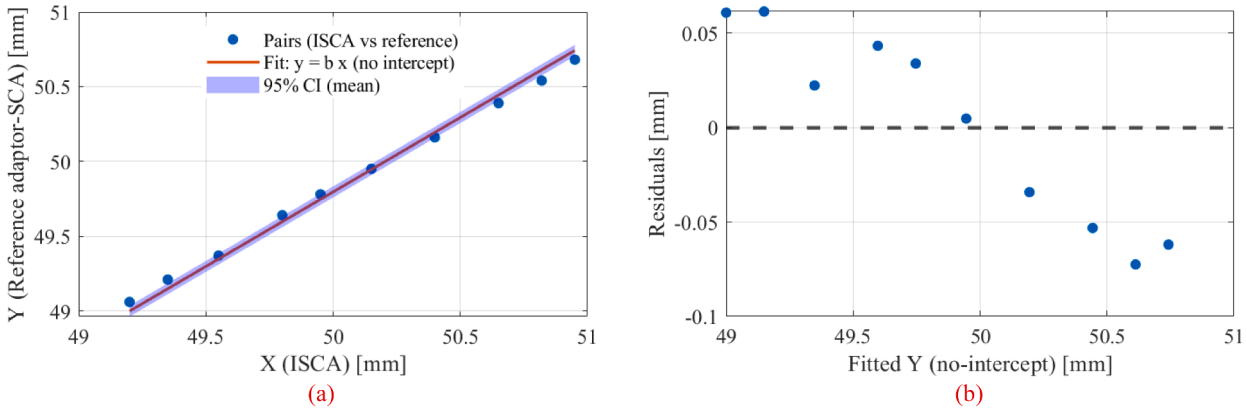

Fig. B. Paired measurements (ISCA vs reference), through-origin least-squares fit and 95% CI for the mean response (a); (b) Residuals versus fitted values for the through-origin model (dashed zero line).

Appendix C. Comparison of Error Evaluation and Compensation Capabilities Among Different Measurement Schemes

To support the comparative analysis conducted in this study, Table C summarizes the differences among three measurement and compensation strategies: ballbar-based radial error evaluation, 2D-projected laser tracker implementation, and full 3D laser tracker modeling. These methods differ in how spatial information is utilized, which axes are involved in the compensation, and how they respond to directional observability constraints.

In this study, all experiments were carried out on circular tool center paths constrained to the YZ plane. Under this configuration, the radial error is inherently defined within the YZ plane, and deviations along the X-axis are not directly involved in the machining path or cutting profile. Therefore, the compensation strategy based on YZ components was sufficient to reduce profile deviation in the planar cutting case considered here.

The ballbar system measures changes in distance along a single direction and is inherently affected by blind direction limitations. The 2D laser tracker implementation used in this study retains the high-resolution spatial data for circle fitting but restricts compensation to the YZ plane to ensure a fair and controlled comparison with the ballbar. Although the laser tracker provides full 3D coordinate data, compensation along the X-axis was not applied in this implementation.

Nevertheless, the full 3D data from the laser tracker remains available and may be exploited in future studies involving more complex spatial paths, 3D volumetric distortion, or multi-axis machine calibration tasks. Such extensions could reveal additional insights into cross-axis coupling and trajectory deviations outside the measurement plane.

Table C
Comparison of error evaluation and compensation strategies.

Category	Ballbar Method	Laser Tracker (2D Projection)	Laser Tracker (Full 3D – Future Work)
Data Dimension	1D projection (along ballbar axis)	3D acquisition, 2D radial projection	Full 3D spatial coordinates
Fitting Method	2D least-squares fitting	3D least-squares circle fit	3D least-squares circle fit
Radial Error Definition	Ballbar length variation	Distance to 3D center, projected onto YZ	Spatial radius to fitted center
Compensation Axes	Y and Z only	Y and Z only	X, Y, and Z (planned)
Blind Direction Effect	Present (unobservable components)	Present (projection enforced)	Eliminated via 3D observability
Applicability in This Study	Active	Active	Not yet applied
Use Case Justification	Valid for planar motion	Matched to ballbar for fair comparison	Future extension for full-space evaluation

Appendix D. Alignment robustness test of the ISCA

To assess the alignment robustness of the ISCA, a repeatability experiment was conducted using a traceable 50 mm calibration plate (calibrated value of 50.0037 mm). The ballbar was first zeroed on the calibration plate, and the ISCA was then completely dismounted and reinstalled ten times. After each reinstallation, the adaptor was returned to the same calibration plate position without re-zeroing, and the ballbar reading L(i) was recorded.

For data processing, the first measurement after zeroing L(1) was taken as the reference. All subsequent readings were expressed as relative offsets:

$$\Delta L(i) = L(i) - L(1),\ \mathrm{i} = 2,\ 3,\ \ldots, 10 \tag{D1}$$

This normalization ensures that the analysis captures only the variation introduced by repeated dismounting and reinstallation, consistent with the relative nature of the ballbar sensor.

The results are summarized in Fig. D. The box plot (Fig. D (a)) shows that all offsets remained within ±7 μm, with a median value of about 4 μm and an interquartile range of approximately 2 μm. This narrow distribution indicates that repeated mounting introduced negligible variation. The trial-by-trial plot (Fig. D (b)) further illustrates the measurement sequence. After the initial runs close to zero, the offsets stabilized around 4-5 μm, with the maximum deviation not exceeding 6.9 μm. The overall peak-to-peak spread was 7.3 μm, and the standard deviation was 2.3 μm. These values are well below 0.01 mm, confirming that the ISCA maintains stable alignment and high repeatability under practical use.

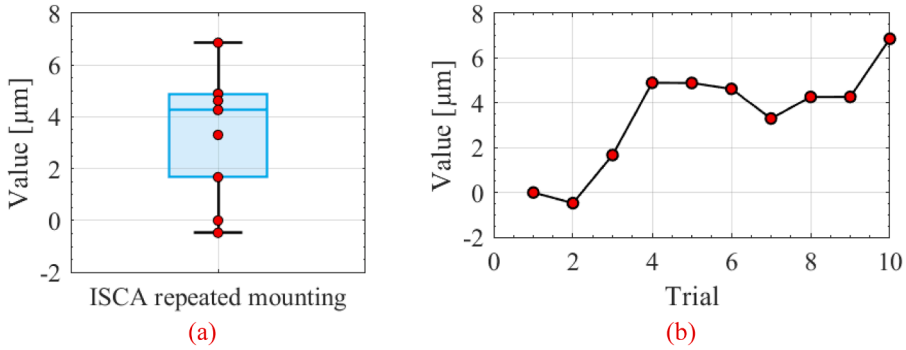

Fig. D. Results of the alignment robustness test of the ISCA on the 50 mm calibration plate: (a) box plot of relative offsets ΔL from ten dismount–remount trials, showing all values within ±7 μm; (b) trial-by-trial plot of ΔL, with a maximum deviation of 6.9 μm and a peak-to-peak of 7.3 μm.

Appendix E. Evaluation of out-of-plane (X-Direction) motion during part machining using laser tracker

To further verify the planarity of the circular trajectories, an additional analysis was conducted using laser tracker based compensation during part machining. The laser tracker provided full 3D coordinate data of the tool center path at different radii, from which the X-direction deviation (perpendicular to the commanded YZ plane) was extracted. Table E summarizes the statistical results, including the mean, standard deviation (STD), peak-to-peak amplitude (P2P), and maximum single-sided deviation (Peak) for six representative trajectories.

Table E
X-direction deviations of circular trajectories measured by laser tracker.

No.	Tool path radius [mm]	Mean [mm]	STD [mm]	P2P [mm]	Peak [mm]
1	47.6	4.81E-14	0.02237	0.082847	0.042893
2	45.4	-8.79E-16	0.02158	0.09619	0.05051
3	40.4	-2.65E-14	0.018801	0.072948	0.037993
4	40.2	-1.64E-14	0.01797	0.069026	0.03632
5	39.6	1.08E-13	0.018937	0.070643	0.036609
6	35.2	7.74E-14	0.016257	0.072281	0.036732

The results show that the X-direction mean deviation was essentially zero for all cases, indicating no systematic drift. The standard deviation ranged from 0.016 to 0.022 mm, while the peak-to-peak amplitude remained below 0.10 mm, with the maximum single-sided deviation less than 0.05 mm. Compared with the in-plane radial errors (typically several tens of microns), the out-of-plane deviations were of smaller or comparable magnitude.

It should be noted that although the X-direction out-of-plane deviations are relatively small (within ±0.05 mm), they can still influence the overall compensation performance, since ballbar measurements are insensitive to components orthogonal to its axis. Nevertheless, the projection of such small X-direction deviations onto the ballbar axis is negligible compared to the in-plane radial errors, meaning their effect on the actual ballbar readings is minimal. Therefore, under the tested conditions, circular trajectories can be regarded as essentially planar.

Appendix F. Verification of Out-of-plane Ballbar measurement on a FANUC serial robot

To assess the applicability of the proposed out-of-plane ballbar measurement and compensation strategy to other robotic systems, experimental validation was carried out on a six-degree-of-freedom serial manipulator (FANUC LR Mate 200iD, see Fig. F (a). The testing conditions were set to closely match those used for the hexapod platform, including a circular trajectory with a 50 mm radius, a feed rate of 1200 mm/min, clockwise motion, and 720 control points per cycle. For each specified radius, three measurement trials were executed to ensure repeatability.

Fig. F (b) illustrates the raw ballbar signals obtained from the serial robot moving in the clockwise direction for radii R50, R48, and R45 (denoted by suffixes “-a/-b”). The traces display a prominent periodic component with consistent phase across repeated measurements, indicating that the primary errors originate from structural factors rather than stochastic noise. As the tested radius decreases, leading to a larger effective out-of-plane angle, both the peak-to-peak amplitude and the low-frequency undulation of the signal increase. This trend aligns with projection-related distortions and axial leakage effects induced by greater angular deviation. Fig. F (c) compares the circular deviation before compensation (BC, shown in blue) and after compensation (AC, shown in orange). For radii ranging from R50 to R45, BC values lie approximately between 486.4 μm and 541.3 μm, whereas AC values are significantly reduced to the 145.7–197.9 μm range, accompanied by low standard deviation, indicating strong repeatability. These improvements correspond to compensation rates between 60% and 71.8% depending on the radius. Fig. F (d) presents the compensation rate as a function of the out-of-plane angle α, with bracketed values indicating the associated measured radius. A monotonic decline in compensation effectiveness is observed as α increases: the highest performance is achieved near α ≈10°, while at α≈30°, the compensation rate falls to approximately 59.3%. This angular dependency is consistent with the projection-based analysis in the main text, where increased α not only enhances in-plane distortion but also introduces greater axial interference into the radial measurement.

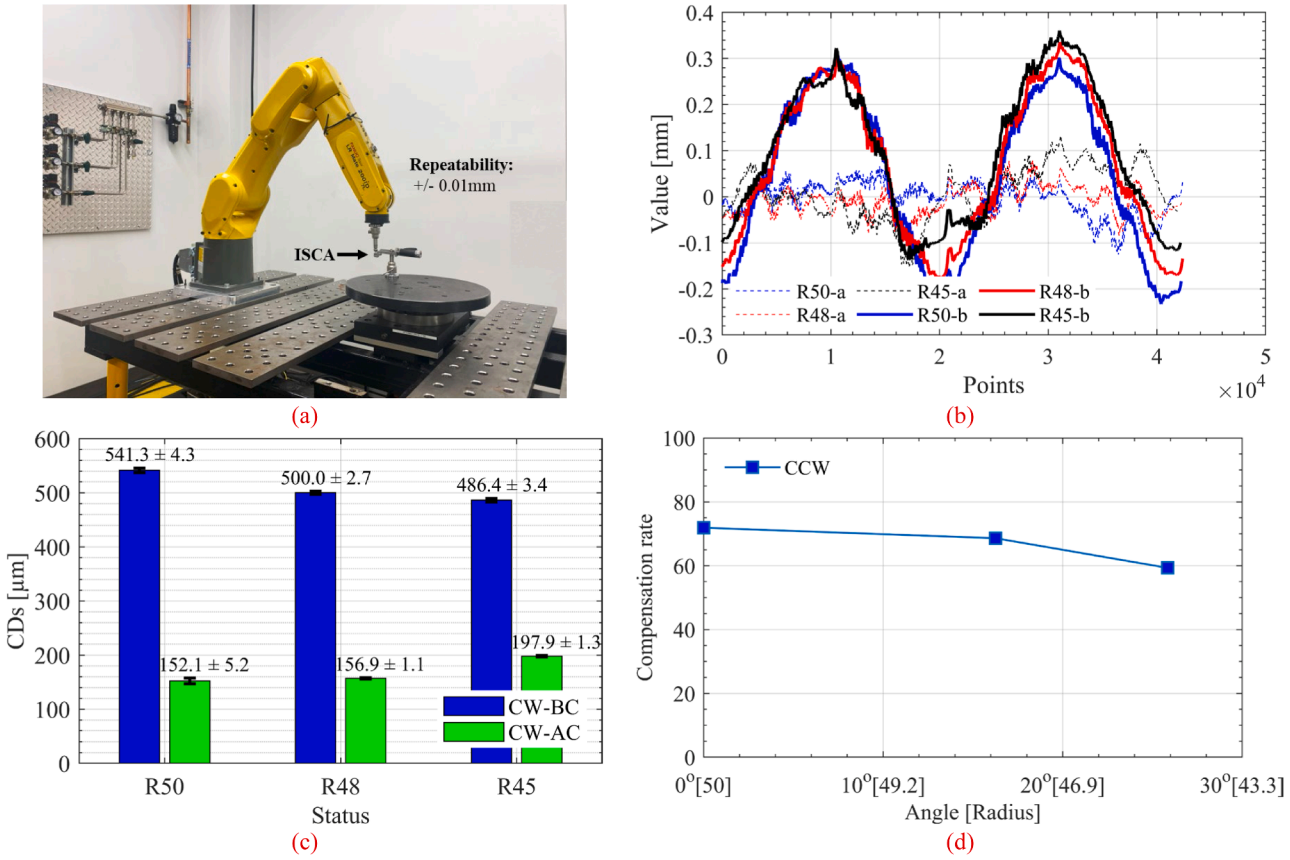

Fig. F. Ballbar measurements at a radius of 50 mm and associated results obtained using the FANUC serial robot (LR Mate 200iD). (a) Experimental configuration for out-of-plane ballbar testing on the serial robot; (b) Raw ballbar signals in the clockwise (CW) direction at radii R50, R48, and R45. For each radius, "-b" denotes the signal before compensation, and "-a" denotes the signal after compensation; (c) Circular deviations (CDs) recorded before (BC) and after (AC) compensation for different radii; (d) Compensation rate plotted as a function of out-of-plane angle α, where bracketed values indicate the corresponding measured radius.

These results indicate that, when α is maintained at or below 30°, the serial robot can sustain a stable compensation rate of approximately 60–70%, which is within 10-15% of the performance achieved with the hexapod under similar conditions. The ballbar measurements confirm the robustness of the proposed compensation approach in mitigating dominant radial errors, demonstrating its applicability across both parallel and serial robotic architectures, provided that axial disturbance is adequately controlled through angle limitation.

Appendix G. Contextual comparison of other measurement approaches

This appendix positions the proposed out-of-plane ballbar approach relative to widely used optical and laser-based metrology solutions. Table G compares three representative categories-ballbar, laser tracker, and stereo-camera/optical photogrammetry-in terms of cost, accuracy, deployment complexity, sensing dimension, and their main advantages and limitations. The values are indicative and intended for contextual reference rather than brand-specific benchmarks.

Table G
Comparison of representative circular-path error measurement methods.

Method	Accuracy	Deployment complexity	Cost	Main pros	Main cons
Proposed out-of-plane ballbar method	Sub-micron sensor resolution; effective error few μm for α ≤ 30°	Moderate	Low–Medium	Low cost; compact; high sampling rate (1000 Hz); direct link to compensation	Sensitive to out-of-plane angle; only 2D projection
Laser tracker	~8-10 μm (3D absolute accuracy)	High	High (>100k USD)	Gold standard for robot/machine calibration; volumetric accuracy	Very expensive; bulky; requires line-of-sight
Stereo-camera / Optical photogrammetry	Tens of μm (baseline- and calibration-dependent)	High	Medium–High (~40–60k USD)	Real-time dynamic tracking; flexible coverage	Sensitive to lighting, occlusion, vibration; requires careful calibration

As summarized in Table G, the proposed out-of-plane ballbar method offers a distinct balance among cost, accuracy, and deployment complexity. While laser trackers remain the benchmark for high-precision 3D metrology and stereo-camera systems provide flexible dynamic tracking, both are costly and demand complex deployment conditions. In contrast, the ballbar-based approach delivers sub-micron sensing resolution and compensation performance comparable to a laser tracker within the 35–50 mm range, at a fraction of the cost and with simpler integration. This positions the method as a practical alternative for shop-floor circular-path error compensation, especially in scenarios where moderate accuracy, low cost, and ease of

deployment are prioritized.

Data availability

Data will be made available on request.

References

[1] D. Zhu, X. Feng, X. Xu, Z. Yang, W. Li, S. Yan, H. Ding, Robotic grinding of complex components: A step towards efficient and intelligent machining – challenges, solutions, and applications, Robot Comput. Integrated Manuf. 65 (2020) 101908.

[2] J.H Jang, S.H Kim, Y.K Kwak, Calibration of geometric and non-geometric errors of an industrial robot, Robotica 19 (3) (2001) 311–321.

[3] Y. Lin, H. Zhao, H. Ding, Real-time path correction of industrial robots in machining of large-scale components based on model and data hybrid drive, Robot Comput. Integrated Manuf. 79 (2023) 102447.

[4] J. Belchior, M. Guillo, E. Courteille, P. Maurine, L. Leotoing, D. Guines, Off-line compensation of the tool path deviations on robotic machining: Application to incremental sheet forming, Robot Comput. Integrated Manuf. 29 (4) (2013) 58–69.

[5] X. Shi, F. Zhang, X. Qu, B. Liu, An online real-time path compensation system for industrial robots based on laser tracker, Int. J. Adv. Robot. Syst. 13 (5) (2016) 1729881416663366.

[6] R. Li, N. Ding, Y. Zhao, H.e Liu, Real-time trajectory position error compensation technology of industrial robot, Measurement 208 (2023) 112418.

[7] R. Holden, P. Lightowler, S. Andreou, Robot Accuracy: Offline Compensation (EU COMET Project), SAE Int. J. Aerospace 7 (2) (2014) 269–273.

[8] A. Verl, A. Valente, S. Melkote, C. Brecher, E. Ozturk, L.T Tunc, Robots in machining, CIRP Ann-Manuf. Technol. 68 (2) (2019) 799–822.

[9] Z. Wang, R. Zhang, P. Keogh, Real-Time Laser Tracker Compensation of Robotic Drilling and Machining, J. Manuf. Mater. Process. 4 (3) (2020) 1–26.

[10] C. Möller, H.C Schmidt, P. Koch, C. Böhlmann, S.-M. Kothe, J.ö Wollnack, W. Hintze, Machining of large scaled CFRP-Parts with mobile CNC-based robotic system in aerospace industry, Procedia Manuf. 14 (2017) 17–29.

[11] S. Ferrarini, P. Bilancia, R. Raffaeli, M. Peruzzini, M. Pellicciari, A method for the assessment and compensation of positioning errors in industrial robots, Robot Comput. Integrated Manuf. 85 (2024) 102622.

[12] T. Shu, S. Gharaaty, W. Xie, A. Joubair, I.A. Bonev, Dynamic Path Tracking of Industrial Robots With High Accuracy Using Photogrammetry Sensor, IEEE/ASME Trans. Mechatron. 23 (3) (2018) 1159–1170.

[13] S. Gharaaty, T. Shu, A. Joubair, W.F Xie, I.A Bonev, Online pose correction of an industrial robot using an optical coordinate measure machine system, Int. J. Adv. Robot. Syst. 15 (4) (2018) 1729881418787915.

[14] T.A. Khaled, O. Akhrif, I.A. Bonev, Dynamic Path Correction of an Industrial Robot Using a Distance Sensor and an ADRC Controller, IEEE/ASME Trans. Mechatron. 26 (3) (2021) 1646–1656.

[15] K. Xing, I.A. Bonev, Z. Liu, H. Champliaud, Positioning performance of a hexapod machining cell under machining and nonmachining operations, J Mech Sci Tech 38 (11) (2024) 6205–6224.

[16] ÅBjörck, Numerics of Gram-Schmidt orthogonalization, Linear. Algebra Appl. 197-198 (1994) 297–316.

[17] C. Rossi, S. Savino, Robot trajectory planning by assigning positions and tangential velocities, Robot Comput. Integrated Manuf. 29 (1) (2013) 139–156.

[18] E. Kelekci, S. Kizir, A novel tool path planning and feedrate scheduling algorithm for point to point linear and circular motions of CNC-milling machines, J. Manuf. Process. 95 (2023) 53–67.

[19] X. Broquere, D. Sidobre, I. Herrera-Aguilar, Soft motion trajectory planner for service manipulator robot, in: 2008 IEEE/RSJ international conference on intelligent robots and systems, IEEE, 2008, pp. 2808–2813.

[20] H. Gattringer, A. Mueller, M. Oberherber, D. Kaserer, Time-optimal robotic manipulation on a predefined path of loosely placed objects: Modeling and experiment, Mechatronics 84 (2022) 102753.

[21] J. Somlo, A. Loginov, Energetically optimal cruising motion of robots, in: Proceedings of IEEE International Conference on Intelligent Engineering Systems, 1997, pp. 333–337.

[22] X. Gao, G. Wang, C. Yun, D. Hao, A calibration method of robot base frame with procrustes analysis, J. Harbin Inst. Technol. 24 (6) (2017) 67–72.

[23] W. Gao, S. Ibaraki, M. Alkan Donmez, D. Kono, J.R.R. Mayer, Y.-L. Chen, K. A. Szipka, A. Archenti, J.-M. Linares, N. Suzuki, Machine tool calibration: Measurement, modeling, and compensation of machine tool errors, Int. J. Mach. Tool Manufact.187 (2023) 1–61.

[24] M.-A. Slamani, A. Nubiola, I.A. Bonev, Assessment of the positioning performance of an industrial robot, Ind. Rob. 39 (2012) 57–68.

[25] K. Xing, I.A. Bonev, H. Champliaud, Z. Liu, Optimizing dynamic measurement accuracy for machine tools and industrial robots with unscented Kalman filter and particle swarm optimization methods, Measure. Sci. Technol. 35 (8) (2024) 085601.